Peer-reviewed version available at *Atmosphere* **2019**, *10*, 653; doi:10.3390/atmos10110653

Dust Storm Event of February 2019 in Central and East Coast of Australia and Evidence of Long-Range Transport to New Zealand and Antarctica

Hiep Duc Nguyen [1,2,3,*], Matthew Riley [1], John Leys [1] and David Salter [1]

[1] Department of Planning, Industry and Environment, New South Wales, PO Box 29, Lidcombe, NSW, Australia

[2] Environmental Quality, Atmospheric Science and Climate Change Research Group, Ton Duc Thang University, Ho Chi Minh City, Vietnam, E-mail: nguyenduchiep@tdt.edu.vn

[3] Faculty of Environment and Labour Safety, Ton Duc Thang University, Ho Chi Minh City, Vietnam

* Corresponding: hiep.duc@environment.nsw.gov.au

Abstract

Between 11 to 15 February 2019, a dust storm originating from Central Australia with persistent westerly and south westerly winds caused high particle concentrations at many sites in the state of New South Wales (NSW), both inland and along the coast. The dust continued to be transported New Zealand and to Antarctica in the south east. This study uses observed data and the WRF-Chem Weather Research Forecast model based on GOCART-AFWA (Goddard Chemistry Aerosol Radiation and Transport – Air Force and Weather Agency) dust scheme and GOCART aerosol and gas-phase MOZART (Model for Ozone And Related chemical Tracers) chemistry model to study the long-range transport of aerosols for the period 11 to 15 February 2019 across eastern Australia and onto New Zealand and Antarctica. Wild fires also happened in northern NSW at the same time and their emissions are taken into account in WRF-Chem model by using Fire Inventory from NCAR (FINN) as emission input.

Modelling results by the WRF-Chem model show that for the Canterbury region of South Island of New Zealand, peak concentration of PM_{10} (and $PM_{2.5}$) as measured on 14 February 2019 at 05:00 UTC at the monitoring stations of Geraldine, Ashburton, Timaru and Woolston (Christchurch) and at Rangiora, Kaiapoi about 2 hours later, correspond to the prediction of high PM_{10} due to intrusion of dust to ground level from transported dust layer above. The Aerosol Optical Depth (AOD) observation data from MODIS 3km Terra/Aqua and CALIOP lidar measurements on board CALIPSO (Cloud-Aerosol Lidar and Infrared Pathfinder Satellite Observations) satellite also indicate that high altitude of dust from 2km to 6km, originated from this dust storm event in Australia, was located above Antarctica.

This study suggests that present dust storms in Australia can transport dust from sources in Central Australia to the Tasman sea, New Zealand and Antarctica.

Keywords: dust transport; Australia; Tasman Sea; New Zealand; Antarctica; WRF-Chem; CALIPSO; MODIS

1. Introduction

Dust aerosols in the atmosphere can affect the weather by acting as condensation nuclei forming cloud, scattering and absorption of incoming solar radiation and hence influence the climate [1]. Dust storms travel long distances and impact the regions downwind [2]. In Australia, dust storms frequently occur from deserts in central Australia (including Simpson, Gibson, Great Victoria and Sturt deserts) [3] and from agricultural land that has been in prolonged drought in western South Australia, Queensland, Victoria and New South Wales (NSW) [4]. As they traverse inland cities and those along the eastern seaboard of Australia, they occasionally affect air quality in these population centres [5] [2].

Australia is a dry continent with vast desert inland in central Australia. In their study of global distribution of aeolian dust using Global Ozone Chemistry Aerosol Radiation and Transport (GOCART) model from 1981 to 1996, Ginoux et al. 2004 [6] showed that Australia is the third largest source contributing to global dust emission, after North Africa and Asia. But in term of dust emission amount, it is only about 20% of Asia and 7% of North Africa annual emission amount.

Approximately 110 million tons of dust emission from Australia each year transported along 2 main pathways across the continent. The south-east pathway and the north-west pathway with approximately 30 million tons deposited to the Tasman sea and Pacific Ocean off the east coast of Australia [7]. Bowler 1976 [8] describes the two major dust paths above. These dust paths were most active between 25,000 and 13,000 BP. Although dust activity was active between 6000 and 3,000 BP and in the last 2000 years, it has not been at the level of the early Quaternary [8]. Sprigg 1982 [9] identified that there are several wind systems that cause wind erosion and transport dust in multiple directions in south-eastern Australia.

O'Loingsigh et al. 2017 [10] in their study of sources and pathway of dust during the Australian "Millennium Drought" decade (late 1990s to mid-2010) using trajectory analysis have shown that dust storm events mostly occurred in austral spring and summer. Dust transport from the centre of the continent to the Australian east coast is typically induced by the cold front systems from the Southern Ocean. In general, the dust is transport by three wind systems as seen from south to north on the Australian east coast: the Southern Dust Path, below 35°S, due to prefrontal northerlies carrying dust to the south coast of Victoria, the Eastern Dust Path (35°S to 25°S, from Canberra, Sydney to Brisbane) due to the frontal westerlies and the North East Dust Path (25°S to 20°S) due to the postfrontal south westerlies [10].

Recent notable events that impact cities on the eastern seaboard include: the 22nd October 2002 event [4], the "Red Dawn" dust storm event in September 2009 [2], and undocumented events in November 2018 and February 2019. The geomorphic literature also has documented long range dust transport in paleo-environments [11].

Many dust storm events transported and deposited dust into the Tasman sea [12] [13] [14], and can be transported as far as New Zealand [15] [16] [17] [18] and Antarctica [19]. Some records of ice cores obtained from Antarctica showed origins of dust transport from Australia [20] [19]. Long range dust deposition enhances carbon cycling [7], iron fertilising the ocean and promoting phytoplankton growth [21] [22]. Following the results of their study on the dust pathways to the east coast of Australia, O'Loingsigh et al. 2017 [10] suggested that the phytoplankton response to dust deposition in the Great Barrier Reef off Queensland was driven by dust from the North East Dust Path. Phytoplankton response in the Tasman Sea is due to deposited dust from the Eastern Dust Path and dust-induced phytoplankton growth in the Southern Ocean is most likely as a result of dust from the Southern Dust Path.

Dust particle size decreases as distance from downwind increases, due to larger particles such as quartz and feldspar sand have a greater settling velocity than smaller particles of clay minerals [23]. However, some larger size particles, such as giant mineral dust particles (>75 μm) which are not usually modelled have been found far away than expected from sources due to turbulence and uplift in convective system [24].

Dust transport studies have used extensive available sets of data from satellites and ground-based observation. Chen et al. 2016 [25] studied the transport of dust event in March 2010 from Taklimakan and Gobi deserts across China to Korea and Japan using WRF-Chem model, they used Aerosol Optical Depth (AOD) data from AERONET ground network and vertical aerosol extinction coefficients from CALIPSO satellite. Chen et al. 2018 [26] recently studied intercontinental dust transport from two dust storm events in 2015 in North Africa (Sahara-Sahel) and Asia (Taklamakan) deserts to the East and West coast of the U.S. using AOD from MYD04-3k (Aqua) Moderate Resolution Imaging Spectroradiometer (MODIS) level 2 products, AI (Aerosol Index) or Aerosol Optical Thickness (AOT) derived from satellite measurements such as GOES (Geostationary Operational Environmental Satellite system) Aerosols/Smoke Product (GASP), OMI (Ozone Monitoring Instrument) onboard Earth Observing System (EOS), VIIRS (Visible Infrared Imaging Radiometer Suite) aboard the Suomi National Polar-orbiting Partnership (Suomi-NPP). In addition, lidar-measurement of aerosol vertical profile by CALIOP onboard CALIPSO satellite, ground based AERONET of solar radiation and air quality monitoring stations as well as MERRA-2 aerosol reanalysis were also used to characterise the source and long-range transport (LRT) pattern of dust events from North Africa and Asia to the U.S.

The WRF-Chem model has been used with various dust emission schemes by many authors to study the dispersion of dust in the atmosphere from dust sources such as Sahara, Arabian and Central Asian deserts [27] [28] [23] [29] [25] [30] [31] [32] [33]. There are 5 dust emission schemes available in WRF-Chem: GOCART (Georgia Tech/Goddard Global Ozone Chemistry Aerosol Radiation and Transport), AFWA (Air Force Weather Agency) and three of the UoC (University of Cologne) schemes (Shao 2001, Shao 2004 and Shao 2011) [34] [35] [36].

Comparison of these dust emission schemes in WRF-Chem have been conducted recently by many authors such as [37] [29] [38] [31] [33] in their simulation studies of dust emission and dispersion. The prediction from different schemes was compared with observation data such as MODIS AOD. Compared to the simpler GOCART algorithm, the AFWA and Shao schemes generally performed better due to their inclusion of saltation mechanism in generating dust from wind speed. Yuan et al. 2019 [33] suggested that the differences in their results from using different schemes (GOCART, AFWA and Shao2004) depend on the sensitivities of the threshold friction velocity on the surface property of the dust source.

Ma et al. 2019 [39] evaluated dust schemes in four air quality models, CMAQS v.5.2.1, CAMx v6.50, CHIMERE v2017r4 and WRF-Chem v3.9.1 in a simulation study of springtime 4-6 of May 2015 dust storm in East Asia. Three dust schemes in WRF-Chem, two schemes in CMAQS and CHIMERE and one in CAMx were used in the simulation. They found that WRF-Chem, with AFWA dust scheme using seasonal dust source map from Ginoux et al. 2012 [40] and parameter tuning, showed the best performance when compared with observation from ground and satellites (MODIS AOD, CALIPSO) followed by WRF-Chem using UoC_Shao2011 dust scheme.

In this study, the dust event of 12-15 February 2019 is studied with focus on the long-range transport (LRT) patterns of dust across the eastern seaboard of Australia, Tasman Sea and beyond to Antarctica using WRF-Chem model with GOCART/MOZART aerosol chemistry as well as observed MODIS satellite AOD data and aerosol vertical profile from CALIOP lidar. The AOD data from satellites, air quality monitoring data at various stations in Australia and New Zealand, MERRA-2 reanalysis as well as lidar vertical profile of aerosols from CALIOP measurements on board CALIPSO satellite and MODIS AOD data are used for comparisons with modelling results. The CALIOP lidar data is particularly valuable, especially in remote places where there are no ground measurements, and vertical structure of aerosols distribution is required for understanding the tropospheric and stratospheric transport of aerosols.

2. Data and Methods

Preprints (www.preprints.org) | NOT PEER-REVIEWED | Posted: 27 October 2019 doi:10.20944/preprints201910.0304.v1

Peer-reviewed version available at Atmosphere 2019, 10, 653; doi:10.3390/atmos10110653

Data used in this study consists of MODIS Aqua/Terra satellite AOD data, CALIOP lidar vertical structure of aerosols, Fire Inventory from NCAR (FINN), air quality monitoring data from the Department of Planning, Industry and Environment (DPIE) air quality monitoring network in New South Wales and Canterbury Regional air quality monitoring stations in New Zealand. The National Centre for Environmental Prediction (NCEP) Final Analysis (FNL) Reanalysis data provides the boundary and initial meteorological condition to be used in WRF-Chem meteorological and chemistry model.

The MODIS 3km aerosol products MYD04-3k (Aqua) and MOD04-3k (Terra) and MOD08_D3 (Terra), MYD08_E3 (Aqua) products are retrieved from Level-1 and Atmosphere Archive & Distribution System (LAADS) https://ladsweb.modaps.eosdis.nasa.gov. The MODIS MOD08_D3, MYD08_E3 is a level-3 MODIS gridded atmosphere daily global joint product providing 1^o x 1^o degree grid average values while the MYD04-3k and MOD04-3k level 2 products monitor the ambient aerosol optical properties (e.g., optical thickness and size distribution), mass concentration, look-up-table-derived reflected and transmitted fluxes, as well as quality assurance and other ancillary parameters, over the oceans globally and over a portion of the continents. Both are suitable for AOD verification with model prediction. The MOD08_D3 product however is most suitable as it combines both Dark Target (DT) algorithm over ocean and part of the continents and Deep Blue (DB) algorithm over bright surface such as desert.

2.1 Dust emission model

The above data are used in conjunction with dust modelling using WRF-Chem to corroborate and verifying the model performance. There are a number of dust scheme option used in WRF-Chem namely the GOCART (Georgia Tech/Goddard Global Ozone Chemistry Aerosol Radiation and Transport) aerosol scheme, the GOCART with AFWA (Air Force Weather Agency) modification to include saltation flux and the University of Cologne (UoC) based on three different dust emission algorithms (Shao 2001, Shao 2004 and Shao 2011).

The original GOCART model to calculate dust emission for different particle size based on wind speed and soil moisture was described by Ginoux et al. 2001 [41]. The empirical equation to calculate dust flux for each particle bin size p as related to wind speed is given as

$$F_p = \begin{cases} CSs_p\, U^2(U - U_t(D_p,\ \theta_s) & U > U_t(D_p,\ \theta_s) \\ 0 & U \leq U_t(D_p,\ \theta_s) \end{cases} \quad (1)$$

where C is an empirical constant (10^{-6} g s^2m^{-5}), S is a unit dust source strength function or erodibility indicating the availability of particles to be entrained, s_p is the mass fraction of emitting dust from soil class (sand, silt and clay) of size p, U is the wind speed at 10m and $U_t(D_p, \theta_s)$ is the threshold wind velocity over which erosion occurs, D_p is the particle diameter of size p and θ_s is degree of saturation measuring soil moisture.

The C constant as implemented in the WRF-Chem source code to be $0.8x10^{-6}$ gs^2m^{-5}. Eltahan et al. 2018 [31] has used it as a tunable value to closely match the predicted AOD with MODIS AOD measurements. Chen et al., 2018 [26] used the value of 1.2µgs^2m^{-5} to match the MODIS ADO. And Ginoux et al 2012 [40] used C as 10^{-6} g s^2m^{-5} for topographic erodibility and C=1.9 x 10^{-6} g s^2m^{-5} for soil erodibility derived from MODIS Deep Blue Level 2 satellite product.

The unitless source strength constant S as a measure soil erodibility is obtained from map representing fraction of cell area of erodibility bare soil of sand and clay. In WRF-Chem model, the erodibility field is generated in WRF Pre-processor (WPS) using the topographic data before being used in WRF-chem core. S is calculated based on premise that dust material available at low point was the result of alluvial processes [42]

Preprints (www.preprints.org) | NOT PEER-REVIEWED | Posted: 27 October 2019 doi:10.20944/preprints201910.0304.v1

Peer-reviewed version available at Atmosphere 2019, 10, 653; doi:10.3390/atmos10110653

$$S = \left(\frac{z\max - z_i}{z_{max} - z_{min}}\right) \qquad (2)$$

where z_i is the cell i elevation and z_{max} , z_{min} are the maximum and minimum elevation in the surrounding 10^0 x 10^0 area respectively. This topographically-based dust source function (DSF) above was referred to as Ginoux source function by [43].

We acknowledge that this dust source domain (Figure 2b) is an underestimate of the area which actually contributed to the dust plume. This is because during droughts, parts of the landscape that are not topographically low, but have reduced ground cover, become dust sources. These are not accounted for in the WRF Pre-processor WPS). The monthly DustWatch report for February 2019 [44] describes the dust sources in the agricultural land of western New South Wales. Figure 1 shows the total vegetation cover for Australia in February, June, November 2018 and February 2019 as determined by the method of Guerschman et al. 2015 [45]. Values less than 50% are possible source areas. It can be seen from these figures that the drought affected south east Queensland and most of western New South Wales from late 2018 and early 2019 when the dust storm occurred in 11 to 15 February 2019. Extra dust sources from drought-affected areas include part of western NSW near the border with the states of South Australia and Victoria.

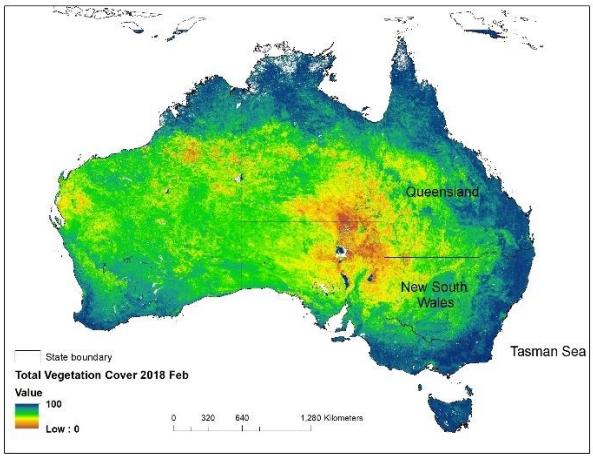

(a)

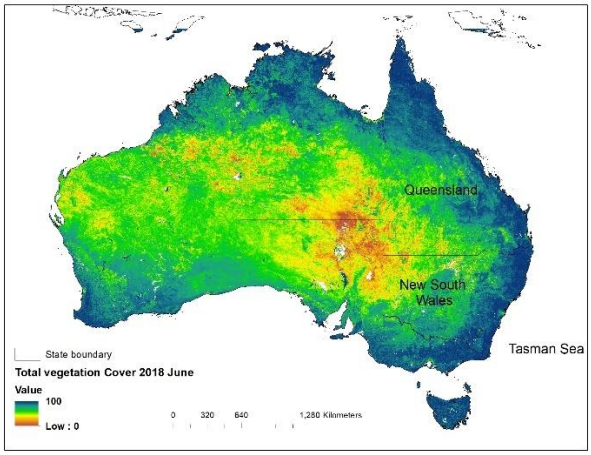

(b)

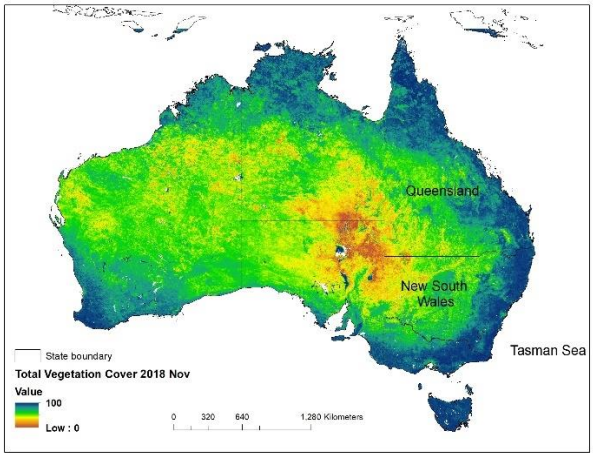

(c)

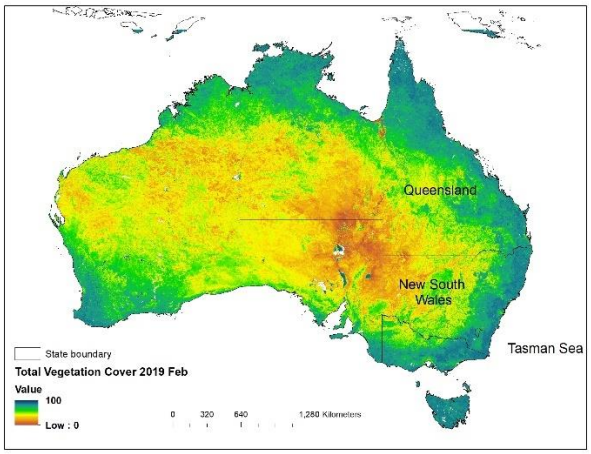

(d)

Figure 1 - Total vegetation cover (%) for Australia in February 2018 (a), June 2018 (b), November 2018 (c) and February 2019 (d) (source: http://www-data.wron.csiro.au/remotesensing/MODIS/products/public/v310/australia/monthly/cover/)

The simple empirical GOCART scheme is popular as it provides a relationship between wind speed and soil characteristics with dust flux emission in a simple equation. The AFWA extension of the GOCART scheme and the UoC schemes (Shao 2001, Shao 2004 and Shao 2011) include the saltation mechanism of dust generation from bombardment of dust particles with various degrees of details. In this study, the GOCART-AFWA scheme is used to study the dust emission and transport from the February 2019 dust storm event. Here we describe the dust emission model of this scheme as implemented in WRF-Chem

The most important variable in equation (1) is the threshold wind velocity. As soil erodibility is depending on soil moisture, the threshold velocity is also adjusted for soil moisture. In the WRF-Chem implementation of GOCART, the threshold velocity however is calculated as a threshold friction velocity based on an equation from Marticorena and Bergametti, 1995 [46]. The Marticorena-Bergametti equation effectively replaces the threshold wind speed U_t used in Ginoux flux equation (1) with threshold friction velocity u_{*t} which was derived in terms of friction velocity u_* rather than wind speed U at 10m

$$u_{*t} = 0.129\,\frac{\left(\frac{\rho_p g D_p}{\rho_a}\right)^{0.5}\left(1+\frac{0.006}{\rho_p g D_p^{2.5}}\right)^{0.5}}{\left[1.928\left(a(D_p)^x+b\right)^{0.092}-1\right]^{0.5}} \qquad (3)$$

where D_p is the diameter of size p particle, g is gravitational acceleration, ρ_p is density of size p particle, ρ_a is air density, x= 1.56, a=1331cm^{-x} and b=0.38.

As Legrand et al 2019 [42] noted, the Marticorena-Bergametti equation was designed for determining the threshold of initiating wind-shear based saltation of grain and not representing the threshold for emission of dust particles from the surface, and hence the AFWA scheme uses it to include the saltation bombardment and particle disaggregation mechanism of dust production.

The AFWA scheme uses a correction factor to account for the effect of soil moisture on threshold friction velocity as

$$u_{*t,s,p} = u_{*t}(D_{s,p})f(\theta) \qquad (4)$$

where

$$f(\theta) = \begin{cases} \sqrt{1+1.21\left(\theta_g-\theta_g{}'\right)^{0.68}} & \theta_g > \theta_g{}' \\ 1 & \theta_g < \theta_g{}' \end{cases} \qquad (5)$$

$D_{s,p}$ is the diameter of saltation size bin p while θ_g is the gravimetric soil moisture fraction and θ_g' is the soil moisture fraction to be absorbed into the soil before capillary forces start to influence the particle disaggregation, and as such is a kind of threshold moisture.

The gravimetric soil moisture is provided from the volumetric soil moisture θ_v by an equation in WRF-Chem

$$\theta_g = \frac{\rho_w \theta_v}{(2.65-0.15c_s)(1-\cdot\phi)} \qquad (6)$$

And

Preprints (www.preprints.org) | NOT PEER-REVIEWED | Posted: 27 October 2019 doi:10.20944/preprints201910.0304.v1

Peer-reviewed version available at Atmosphere 2019, 10, 653; doi:10.3390/atmos10110653

$$\theta_g' = 0.0014(100c_s)^2 + 0.17(100C_s) \qquad (7)$$

where ρ_w is water density which is 1gcm^{-3}, ϕ is the soil porosity, c_s is the soil clay content mass fraction and the term $(2.65 - 0.15c_s)$ represents the soil density.

Once the threshold friction velocity is determined, the horizontal saltation flux is next found to find the bulk dust emission vertical flux

The horizontal saltation flux for particle size of bin p

$$H(D_{s,p}) = \begin{cases} C_{mb}\frac{\rho_g}{g}u^{*3}\left(1+\frac{u^*_{t,s,p}}{u^*}\right)\left(1-\frac{u^{*}{}^2_{t,s,p}}{u^*}\right) & u^* > u^*_{t,s,p} \\ 0 & u^* \le u^*_{t,s,p} \end{cases} \qquad (8)$$

The constant C_{mb} is implemented in GOCART AFWA WRF-Chem model as 1 based on Marticorena and Bergametti 1995 [46], rather than 2.61 of the original equation. Eltahan et al. 2018 [31] has used C_{mb} as a tunable parameter.

In this study, this parameter is also used a tunable constant adjusting it to make the predicted PM_{10} ground dust concentration comparable with PM_{10} observation at monitoring stations. Eltahan et al. 2018 [31] have adjusted this parameter ranging from 1 to 10 in their studies of two dust storm events January 2004 and March 2013 in the deserts of Egypt.

As noted in the WRF-Chem code, the sandblasting efficiency β acts to reduce dust emissions in areas with few dust-sized particles so that the lofting efficiency decreases, otherwise super sandy zones would be huge dust producers [46]. β is between 1x10^{-6} and 1.36 x 10^{-6} cm^{-1} (varying with clay mass fraction from 0 to 1).

And finally, the dust emission flux is calculated for regions which are defined as grassland, sparsely vegetated or barren [42], i.e surface roughness length $z_0 \le 20$cm as

$$F_B = \begin{cases} GS\beta & z_0 \le 20cm \\ 0 & z_0 \ge 20cm \end{cases}$$

The dust emission models above used a number of parametrisation equations with some defined constant variables, such as threshold friction velocity in AFWA and UoC schemes, which can affect the dust emission and the results of dust concentration and the particle transport in different region and in different dust storm simulation cases depending on the characteristic values of these constants. Tuning scales or coefficients have been used in those dust schemes such as GOCART to calibrate the scheme to account for uncertainties in soil characteristics of a particular area and to achieve comparable results with observation data such as AOD [47] [38] [31] [27].

In WRF-Chem, the GOCART-AFWA scheme is implemented with volumetric soil moisture which can be tuned with a dust_smtune option in namelist, such that θ_v in equation (6) has the value θ_v = max (θ_v*smtune, 0)

2.2 Fire emission using FINN and WRF-Chem MOZART gas-phase chemistry

In the New England area of northern NSW, there were extensive large wild fires over the period 10/2/2019 to 15/2/2019. The emission from wild fires affected the air quality in this region and beyond as shown by MODIS Terra/Aqua satellites. To account for this source of emission of both aerosols and gaseous chemical species, the Fire Inventory from NCAR (FINN) emission data of 1 km resolution derived from MODIS Rapid Response fire count (FIRMS) hotspots are used. These data are usually provided in the daily basis and can be downloaded from https://www.acom.ucar.edu/acresp/dc3/finn-data.shtml. We use FINN instead of the Global Fire Emissions Database, Version 3 (GFED v3) as

Preprints (www.preprints.org) | NOT PEER-REVIEWED | Posted: 27 October 2019 doi:10.20944/preprints201910.0304.v1

Peer-reviewed version available at Atmosphere 2019, 10, 653; doi:10.3390/atmos10110653

GFED v3 provides only monthly temporal resolution at 0.5° spatial resolution instead of daily resolution from FINN.

The FINN emission data are prepared with appropriate species for 3 gas-phase chemical mechanism as provided from FINN: GEOS, SAPRC99 and MOZART chemistry. The files provided from FINN are named for each of the chemistry as GLOB_GEOSchem_yyyyJ.txt.gz, GLOB_MOZ4_yyyyJ.txt.gz or GLOB_SAPRC99_yyyyJ.txt.gz where yyyy is the year y and J is the Julian day of the year.

In this study, we use MOZART gas-phase chemistry model as it can be used in conjunction with GOCART aerosol chemistry module in WRF-Chem. The WRF-Chem chemistry option is then MOZART/GOCART (chemp_opt=112).

2.3 WRF-Chem configuration

The WRF-Chem domain for the study consists of the eastern half of Australia, the Tasman sea and New Zealand to adequately cover the region of interests for the dust storm event of February 2019. The National Centre for Environmental Prediction (NCEP) Final Analysis (FNL) Reanalysis data provides the boundary and initial meteorological condition and the default chemical profiles in WRF-Chem for the simulation. Figure 2 shows the domain configuration of 355 east-west grid points and 218 north-south grids of 15km by 15km resolution and 30 vertical levels.

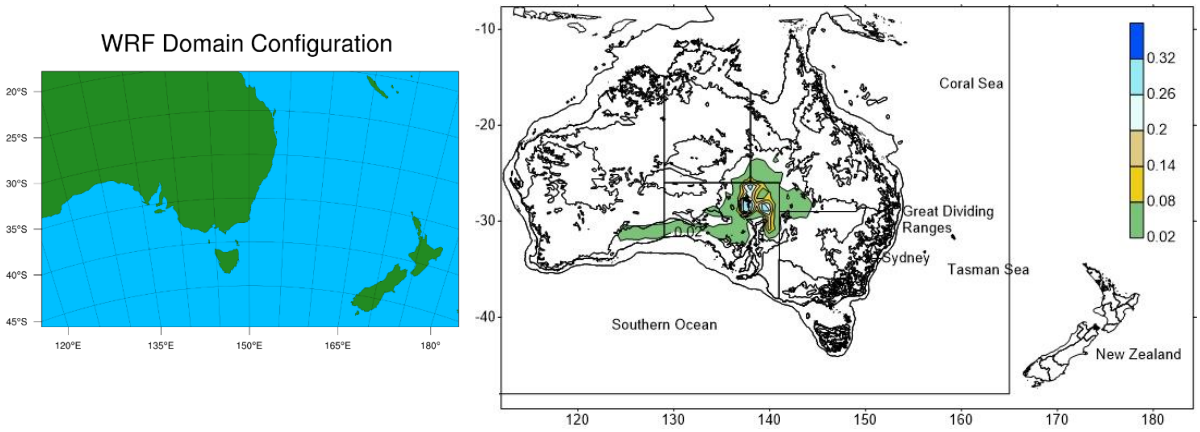

Figure 2 – (a) Modelling domain (Lambert projection) with 15km x 15km resolution (lat from -45.5384° to -17.914°, and longitude from 116.025° to 184.175°). (b) The topographic sand erodibility (0-1) contour map (coloured) within the topography of the Australian continent is used by WRF-Chem dust module to scale the dust flux.

To have aerosol optical properties output (extinction coefficient, extcof55, at 550 nm wavelength), the aerosols chemistry GOCART (chem_opt=300) and output of aerosol extinction coefficient calculated based on Maxwell-Garnett approximation (aer_opt_opt=2) are chosen. As radiative aerosols interactive feedback on meteorology can effect the dust emission as was shown by Wang et al. 2018 [48] and similar to Rizza et al. 2017 [30] who considered the aerosol chemistry GOCART scheme in their study of dust outbreak from Sahara Desert in 2004 and the Maxwell-Garnett rule to derive aerosol properties, this WRF-Chem simulation study of dust event in east coast of Australia also considers the aerosol direct radiative effect using Rapid Radiative Transfer Model (RRTMG) for both short-wave and long wave radiation (ra_sw_physics=4, ra_lw_physics=4). Direct aerosol radiative effect on meteorology using RRTMG were also used by Zhao et al. 2011 [49] and Chen et al. 2014 [28] in their studies of aerosols effect on precipitation in West Africa and dust mass balance from Asian desert dust sources.

The topographic sand erodibility field as shown in Figure 2b is generated from map of sand and clay bare soil and topographic data as represented by Equation 2. The simulated wind speed and soil moisture

Preprints (www.preprints.org) | NOT PEER-REVIEWED | Posted: 27 October 2019 doi:10.20944/preprints201910.0304.v1

Peer-reviewed version available at Atmosphere 2019, 10, 653; doi:10.3390/atmos10110653

in WRF provide the input to WRF-Chem dust emission scheme. The microphysics scheme used is the WRF Single-Moment (WSM) 3-class suitable for mesoscale grid sizes (mp_physics=3) and the surface layer physics is based on Monin-Obukhov similarity scheme (sf_sfclay_physics = 1) which is compatible to the planetary boundary layer (PBL) YSU (Yonsei University) model. While the land surface model used is the Noah Land-Surface Model, a unified NCEP/NCAR/AFWA scheme with soil temperature and moisture in four layers, fractional snow cover and frozen soil physics (sf_surface_physics = 2), the cumulus option is the Kain-Fritsch scheme (cu_physics=1). Table 1 summarises the parametrisation used in namelist setting of WRF-Chem for this study and other relevant dust studies in literature.

Physical parametrisation	Namelist variable	Option	Model/scheme	Other relevant dust studies
Microphysics	mp_physics	3	WRF Single Moment	Chen et al. 2016, Yuan et al. 2019 (two-moment Morrison scheme)
Land surface	sf_surface_physics	2	Noah Land-Surface Model	Cavazos-Guerra and Todd 2012, Zhao et al. 2010, Eltahan et al. 2018, Yuan et al. 2019
Surface layer physics	sf_sfclay_physics	1	Monin-Obukhov similarity	Fountoukis et al. 2016
Planetary Boundary Layer	bl_pbl_physics	1	YSU scheme	Fountoukis et al. 2016, Eltahan et al. 2018, Chen et al., 2018. Yuan et al. 2019
Shortwave radiation	ra_sw_physics	4	Rapid Radiative Transfer Model (RRTMG)	Rizza et al. 2017, Eltahan et al. 2018, Chen et al., 2018, Yuan et al. 2019
Long wave radiation	ra_lw_physics=	4	Rapid Radiative Transfer Model (RRTMG)	Rizza et al. 2017, Fountoukis et al. 2016, Eltahan et al. 2018, Chen et al., 2018, Yuan et al. 2019
Aerosol Chemistry	chem_opt	300 (112)	GOCART (and MOZART/GOCART)	Rizza et al. 2017
Dust scheme	dust_opt	3	GOCART-AFWA scheme	Fountoukis et al. 2016, Yuan et al. 2019
Aerosol extinction	aer_opt_opt	2	Maxwell-Garnett approximation	Rizza et al. 2017

Preprints (www.preprints.org) | NOT PEER-REVIEWED | Posted: 27 October 2019 doi:10.20944/preprints201910.0304.v1

Peer-reviewed version available at Atmosphere 2019, 10, 653; doi:10.3390/atmos10110653

coefficient approximation				
Aerosol radiative feedback	aer_ra_feedback	1	Turn on aerosol radiative feedback with RRTMG model	Wang et al, 2018, Cavazos-Guerra and Todd 2012

Table 1 – Namelist setting in WRF-Chem setup

The GOCART-AFWA has dust particles distributed into 5 bins: bin 1 (particles of size 0-1µm), bin 2 (1.0-1.8µm), bin 3 (1.8-3.0µm), bin 4 (3.0-6.0µm) and bin 5 (6.0-10µm). The effective radius of particle sizes in those bins are 0.5, 1.4, 2.4, 4.5, and 8µm respectively. Particles with radius between 63µm to 2000µm are considered as sand, between 2µm to 63µm as silt and below 2µm as clay particles [50] [31]. The dust fractions in the 5 dust bins are allocated as 0.1024, 0.1012, 0.2078, 0.4817 and 0.1019 respectively [33]. The concentration output is in µg/kg-dry air (which is equal to 1.29 µg/m3 at standard temperature and pressure).

The AOD at 0.55 µm is calculated as

$$AOD = \sum_{i=1}^{n-1} coef55 * \Delta z_i$$

where Δz_i is the i-layer depth (z_i+1 – z_i) and *coef*55, as output from WRF-Chem, is the extinction coefficients for .55µm wavelength.

2.4 Emission data

The biogenic and anthropogenic emission data for WRF-Chem input used in this study are the MEGAN (Model of Emissions of Gases and Aerosols from Nature) and the global 2005 anthropogenic EDGAR (Emission Database for Global Atmospheric Research) version 4 compiled for Task Force on Hemispheric Transport of Air Pollution (TF-HTAP) which has emission sources include land-based and shipping transport at 1°x1° resolution. The EDGAR-HTAP emission data includes fine particulate matter PM_{10} and $PM_{2.5}$, carbonaceous speciation Black Carbon (BC) and Organic Carbon (OC), ozone precursor gases such as Carbon Monoxide (CO), Nitrogen Oxides (NO_x), Non-Methane Volatile Organic Compounds (NMVOC), acidifying gases such as Ammonia (NH_3), Nitrogen oxides (NO_x) and Sulfur Dioxide (SO_2) and greenhouse gases of CO_2, Methane (CH_4) and Nitrous Oxides (N_2O). Figure 3 shows EDGAR_HTAP anthropogenic emission of NO and BC in the modelling domain.

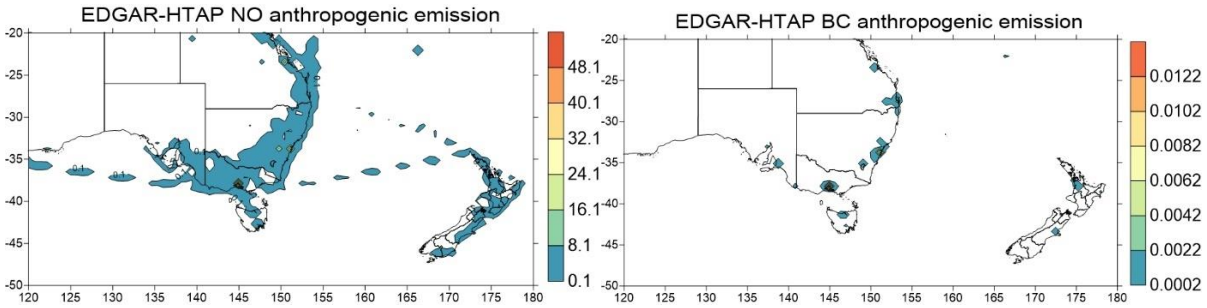

Figure 3 – EDGAR-HTAP global anthropogenic emission of nitrogen monoxide (NO) emission (mol km^{-2} hr^{-1}) and black carbon (BC) emission (µg/m^3 m/s) for February 2019. The emission includes land-based and ocean shipping emission.

3. Results

Figure 4 shows the predicted spatial distribution at level 1 (ground) of dust particle concentration in bin 2 size at 13 February 2019 05:00 UTC (13 February 2019 15:00 AEST) and the following day at 14 February 2019 4:00 UTC (14 February 2019 14:00 AEST or 16:00 NZ) from WRF-Chem GOCART-

Preprints (www.preprints.org) | NOT PEER-REVIEWED | Posted: 27 October 2019 doi:10.20944/preprints201910.0304.v1

Peer-reviewed version available at Atmosphere 2019, 10, 653; doi:10.3390/atmos10110653

AFWA dust model. Peak PM_{10} and $PM_{2.5}$ concentrations were detected at Tamworth and Armidale monitoring sites in the New England region of NSW at 13 February 2019 6:00 UTC (13 February 2019 16:00 AEST) and Bargo, Bringelly, Prospect and other monitoring stations in Sydney region, Australia at 12 February 2019 9:00 UTC (12 February 19:00 AEST) and monitoring sites in Canterbury region of South Island in New Zealand 14 February 2019 5:00 UTC (14 February 2019 17:00 NZ).

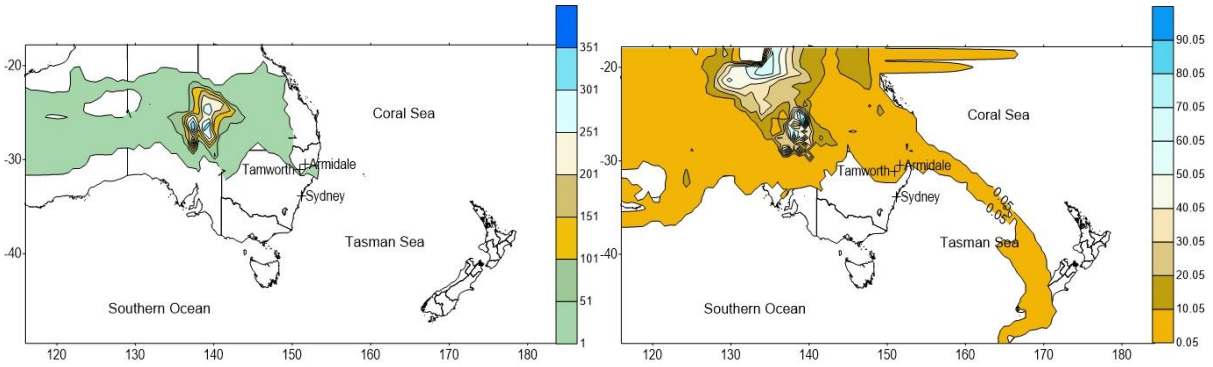

Figure 4 – Dust particles of bin 2 size (1 to 1.8 µm) concentration (µg/kg dry-air) on 13 February 2019 5:00 UTC and 14 February 2019 4:00 UTC.

The predicted temperature and surface wind field from WRF-Chem across the domain show a consistent wind pattern from south westerly on 11 and 12 February 2019 12:00 UTC and to easterly on 13 February 2019 12:00 UTC and 14 February 2019 12:00 UTC with a cold front in the Southern Ocean as shown in Figure 5.

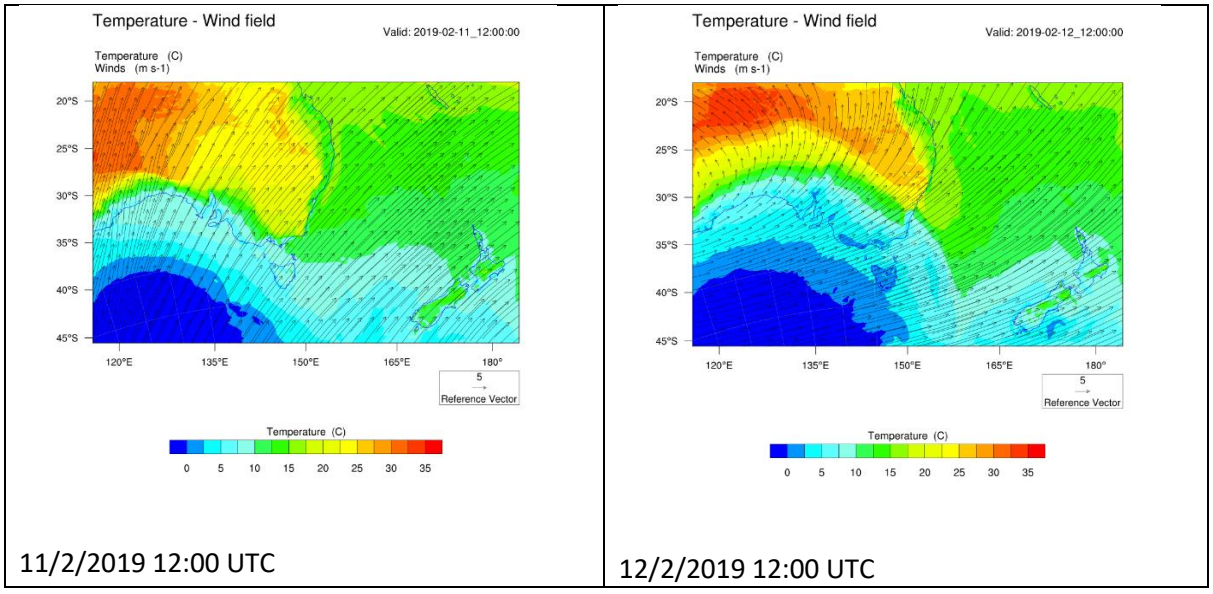

Preprints (www.preprints.org) | NOT PEER-REVIEWED | Posted: 27 October 2019 doi:10.20944/preprints201910.0304.v1

Peer-reviewed version available at Atmosphere 2019, 10, 653; doi:10.3390/atmos10110653

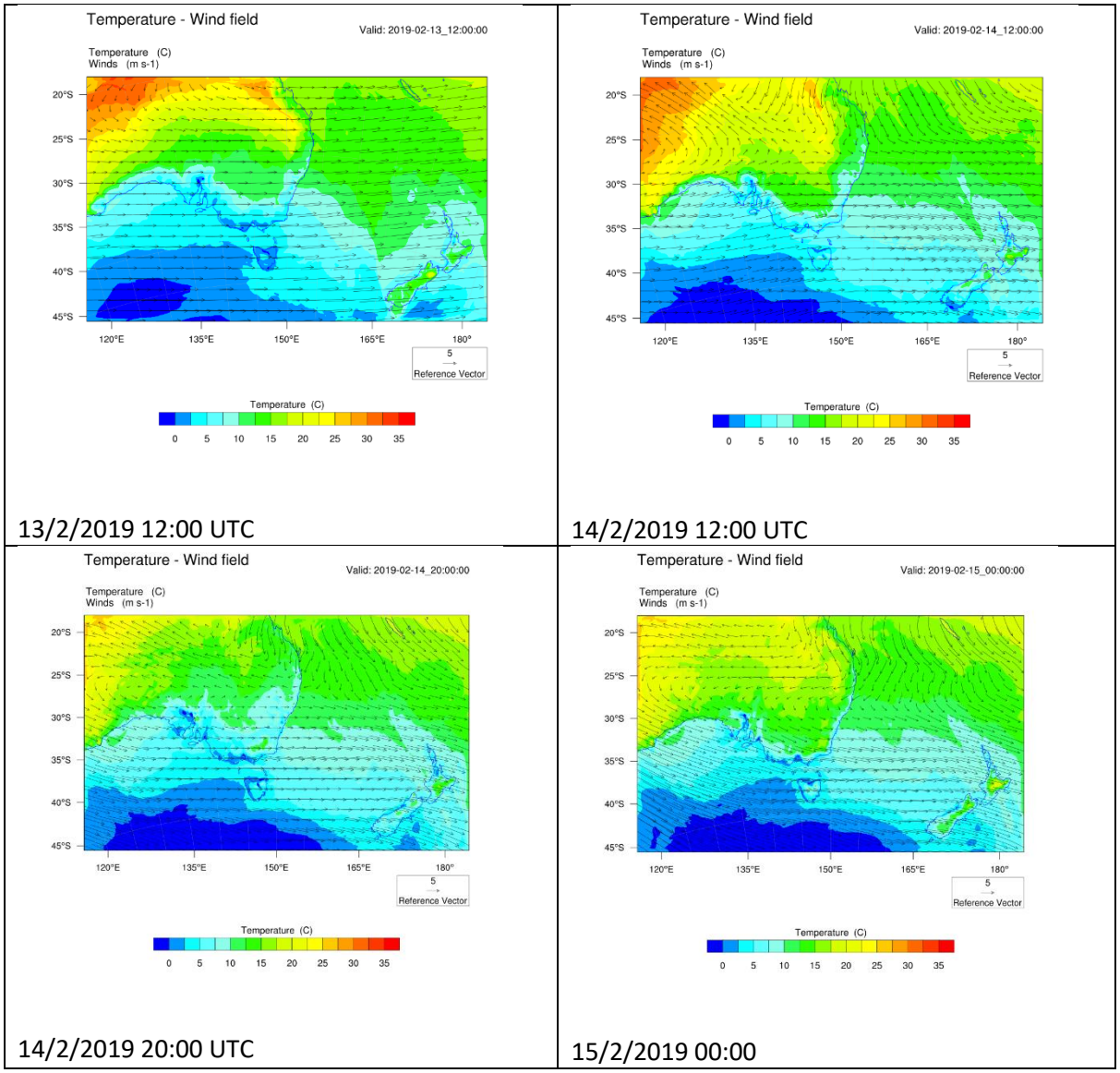

Figure 5 – Surface temperature and wind field across the domain on 11 February 2019, 12 February 2019, 13 February 2019 and 14 February 2019 12:00 UTC. From 14 February 2019 12:00 UTC to 15 February 2019 00:00 UTC, the wind changed from easterly to north easterly at longitude 170 and beyond.

The wind fields at different height and time are also important in understanding the dispersion and transport of dust aerosols. The temperature and wind field at 700, 850 and 925mb (hPa) levels in the lower troposphere on 11 February 2019 and 12 February 2019 at 12:00 UTC is shown in Figure A1 of the Appendix. At 925mb and 850mb, the south westerly flow from the Southern Ocean merged with the easterly flow from the Coral Sea forming a northernly and westerly flow above the Tasman Sea and New Zealand. The wind field pattern at 700mb above the Tasman Sea and New Zealand is similar to those at 925mb and 850mb. For the 13 February 2019 12:00 UTC, the predicted wind from WRF-Chem at 925mb, 850mb and 700mb shows south westerly and southernly flow over Australia continent and northernly and westerly over the Tasman Sea and New Zealand while on 14 February 2019 12:00 UTC the wind fields at 925, 850 and 700mb show an westerly flow over the Southern Ocean and New Zealand and southernly flow above the Tasman Sea (see Appendix Figure A2).

The CALIOP lidar, onboard CALIPSO satellite, detected thick layer of dust (up to 2km above ground level) above central Australia on 11 February 2019 from 4:27 to 4:40 UTC as shown in Figure 6. The

Preprints (www.preprints.org) | NOT PEER-REVIEWED | Posted: 27 October 2019 doi:10.20944/preprints201910.0304.v1

Peer-reviewed version available at Atmosphere 2019, 10, 653; doi:10.3390/atmos10110653

extent of the dust cloud ranged from western New South Wales near the border with Victoria to western Queensland and was approximately 1500 km long.

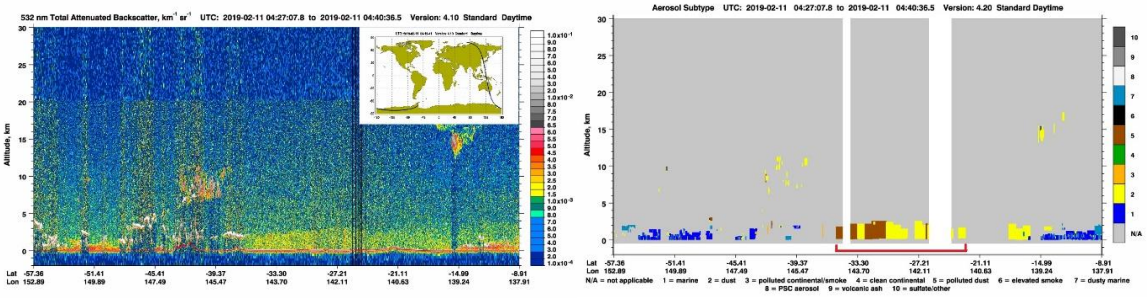

(a) (b)

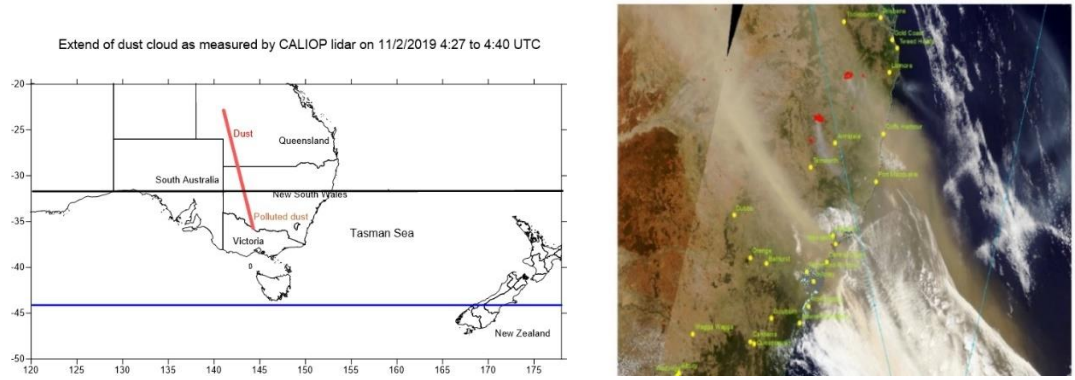

(c) (d)

Figure 6 – Extent of dust cloud as detected by satellites: (a) Lidar 532nm total attenuated backscatter vertical structure on 11 February 2019 from 4:27 to 4:40 UTC with CALIPSO satellite path above central Australia (b) aerosol subtype vertical profile as derived from CALIOP measurements (c) Extent of dust cloud (red line) as measured by CALIPSO satellite on 11 February 2019 4:27 to 4:40 UTC and cross sections of predicted PM_{10} and wind profile (black and blue lines). (d) MODIS Terra satellite image of the dust event and wild fires in the New England area on 13 February 2019 and the locations of the main towns and cities in NSW.

Predicted vertical PM_{10} and wind profiles allow us to understand the process of dispersion and evolution of the dust plumes from emission sources across the modelling domain. The PM_{10} and wind profiles across the -31.73^{o} latitude horizontal line (black line) in Figure 6c at different times are shown in Figure 7. The southwesterly wind carried the dust from the modelled sources in central Australia, the dust plume crossed the Great Dividing Ranges on north westerly winds (Figure 7a) over the coast to the Tasman Sea on southwesterly winds (Figure 7 b, c and d). The vertical wind (w-component) is small compared to the u and v-components above this cross section line.

Preprints (www.preprints.org) | NOT PEER-REVIEWED | Posted: 27 October 2019 doi:10.20944/preprints201910.0304.v1

Peer-reviewed version available at Atmosphere 2019, 10, 653; doi:10.3390/atmos10110653

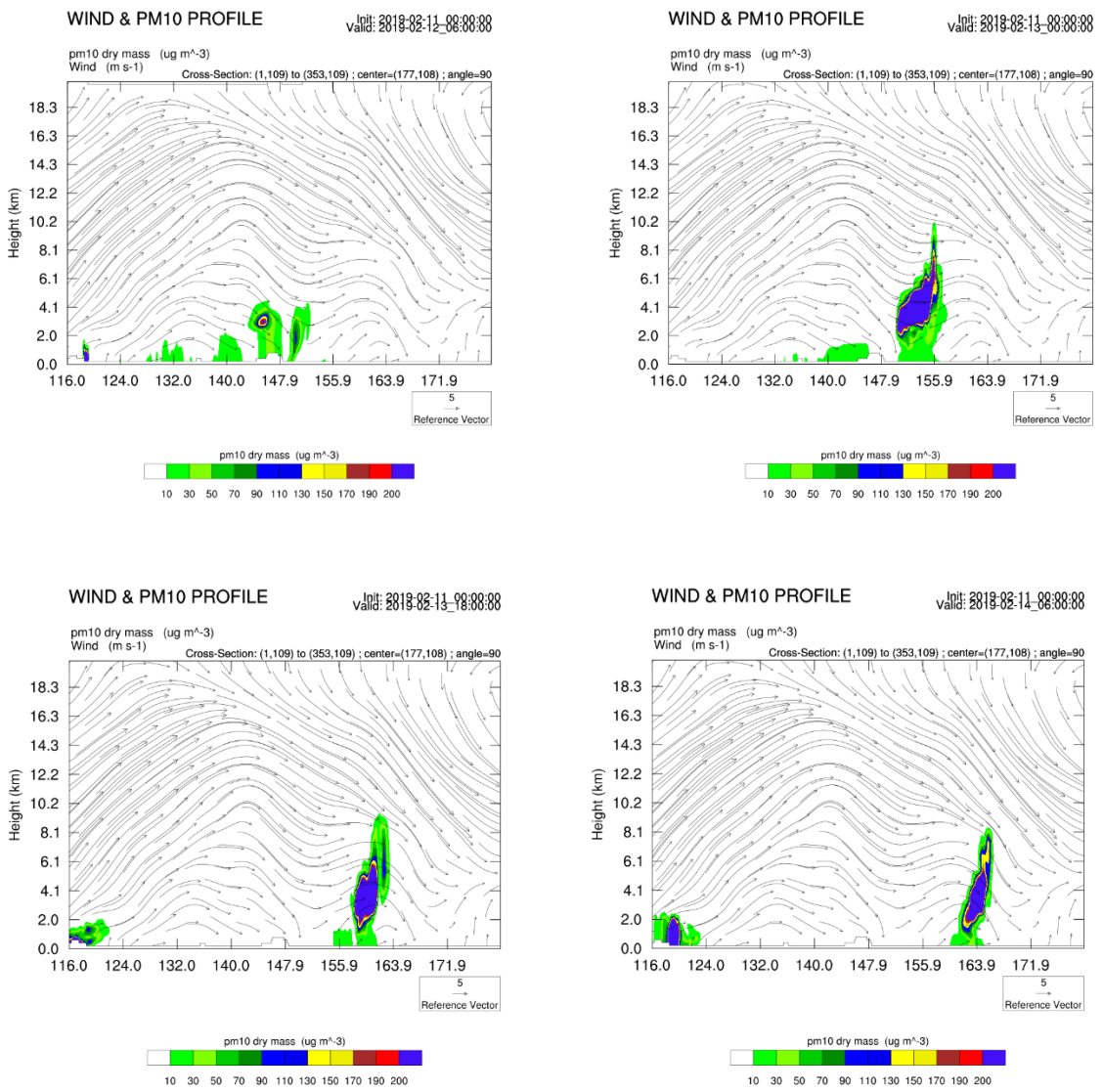

Figure 7 – Predicted PM_{10} and wind profile along the latitude -31.73º at 12 February 2019 06:00, 13 February 2018 00:00, 13 February 2019 18:00 and 14 February 2019 06:00 UTC. The vertical topographic outline at the bottom of the graphs shows the Great Dividing Range in the middle having on the left the western plain and on the right the Tasman Sea.

3.1 Dust transport across the Tasman Sea to New Zealand

Similar to the above vertical cross section across the dust source region in central Australia as shown as horizontal black line in Figure 6c, the cross section below (blue line) in Figure 6c, at latitude -44.10º over the town of Geraldine in New Zealand (Figure 10a), shows that, on the 13 February 2019 at 00:00 UTC, the dust cloud first appeared along this cross section west of NZ South Island. But north and north easterly winds from ground up to 10km prevented the dust cloud from reaching the island until 16:00 UTC on the same day. The dust cloud stayed above the South Island from then until from 14 February 2019 04:00 to 06:00 UTC when it intruded to ground level causing elevated PM_{10} concentration at Geraldine and other sites nearby (Figure 8).

Preprints (www.preprints.org) | NOT PEER-REVIEWED | Posted: 27 October 2019 doi:10.20944/preprints201910.0304.v1

Peer-reviewed version available at *Atmosphere* **2019**, *10*, 653; doi:10.3390/atmos10110653

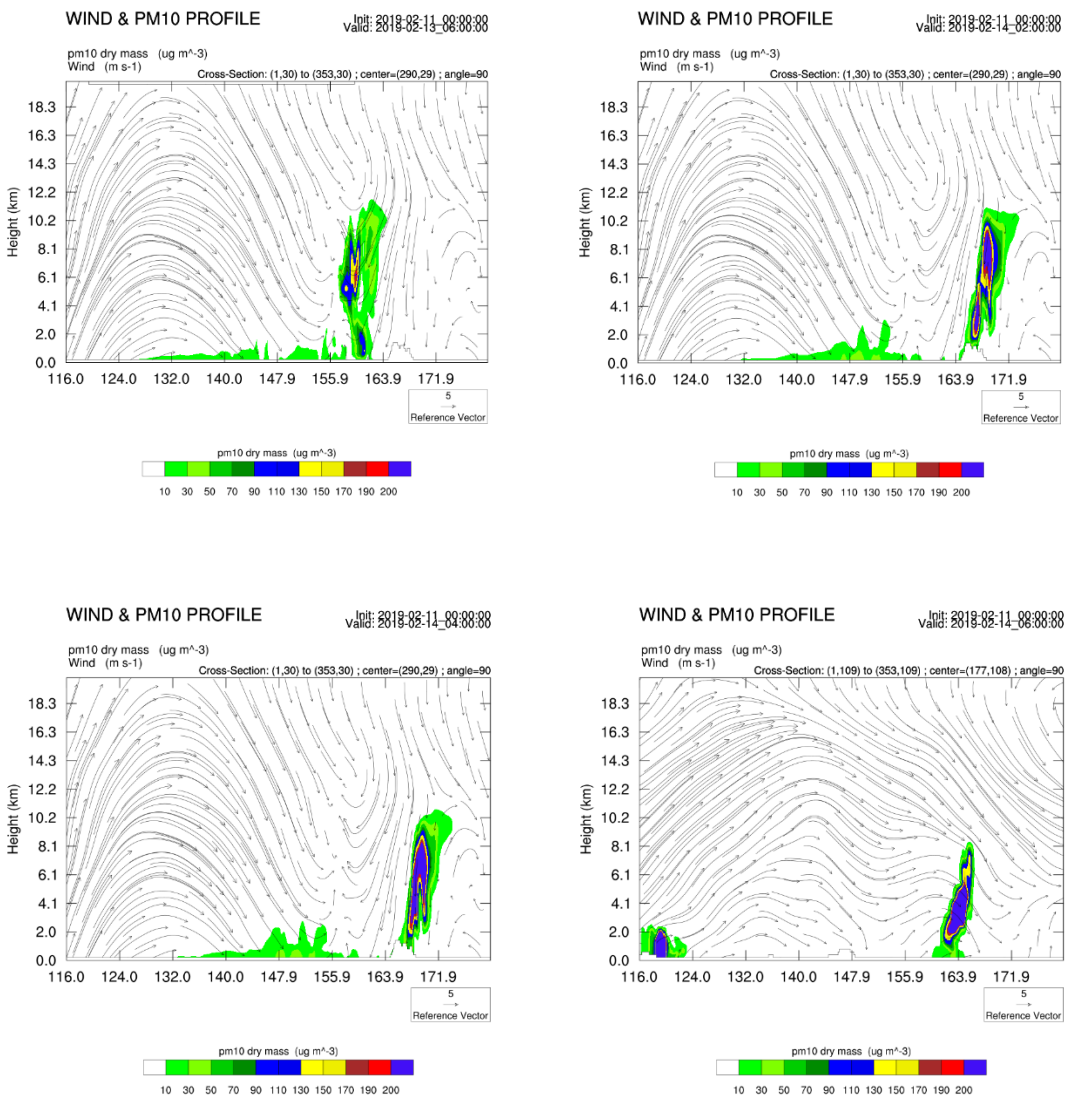

Figure 8 – Predicted PM_{10} and wind profile along the latitude -44.10° at 13 February 2019 06:00, 14 February 2018 02:00, 14 February 2019 04:00 and 14 February 2019 06:00 UTC. The vertical topographic outline at the bottom of the graphs show the Tasman Sea and South Island of New Zealand.

The progress of the dust and smoke plumes as viewed from above can also be seen in the AOD spatial pattern over time as revealed by MODIS Terra/Aqua MO08-D3 and MYD08-E3 satellite product. The AOD from Deep Blue algorithm for bright target on land (such as desert) and the Dark Target algorithm for dark target such as ocean can be combined. These AODs are shown in Figure 9 for the 13 February 2019 from Terra MOD08-D3 product and in Figure A3 of the Appendix for the period from 10 to 17 February 2019 from Aqua MYD08-E3 product. The MYD08-E3 product provides the maximum and average of daily AOD for the 7 days period starting from 10 and ending on 17 February 2019 which show the spatial pattern of AOD for this period as a result of the dust transported in the February 2019 dust storm.

Preprints (www.preprints.org) | NOT PEER-REVIEWED | Posted: 27 October 2019 doi:10.20944/preprints201910.0304.v1

Peer-reviewed version available at *Atmosphere* **2019**, *10*, 653; doi:10.3390/atmos10110653

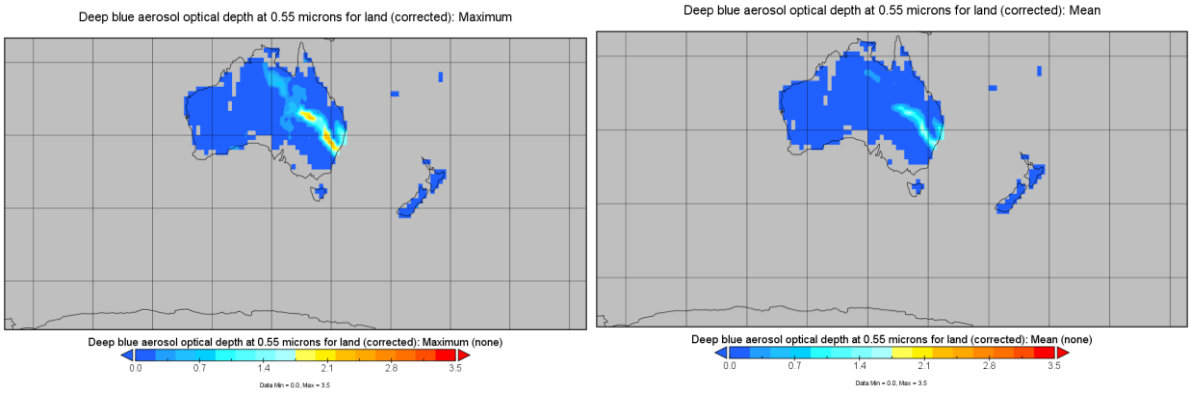

(a)

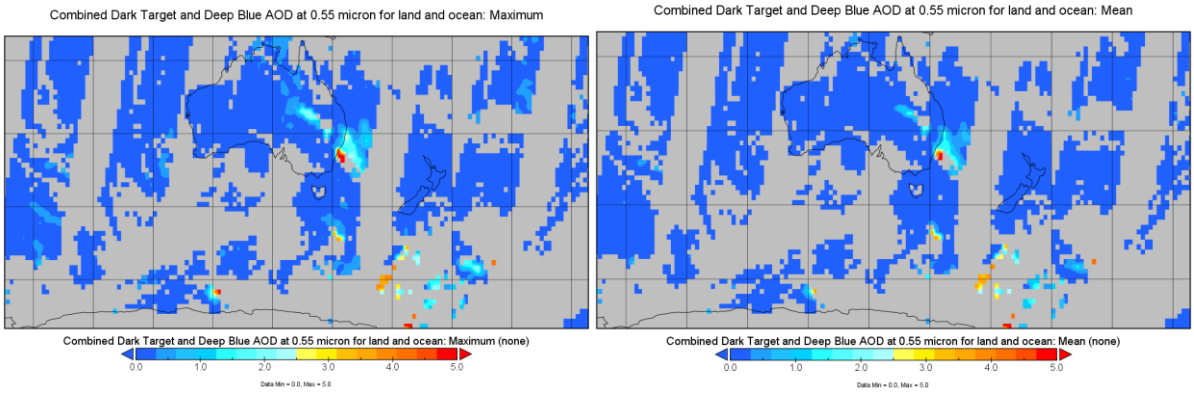

(b)

Figure 9 – (a) Maximum and mean AOD Deep Blue Terra MOD08-D3 for the 13 February 2019 and (b) Combined maximum and mean AOD of Deep Blue (land) and Dark Target (ocean) from Terra MOD08-D3 for 13 February 2019

At monitoring sites in the Canterbury region of South Island of New Zealand such as Geraldine, Timaru and Woolston (Christchurch) which are more than 100km from each other, peak concentrations of PM_{10} (and $PM_{2.5}$) were detected on 14 February 2019 05:00 UTC and at Rangiora, Kaiapoi about 2 hours later. The locations of these air quality sites are shown in Figure 10a.

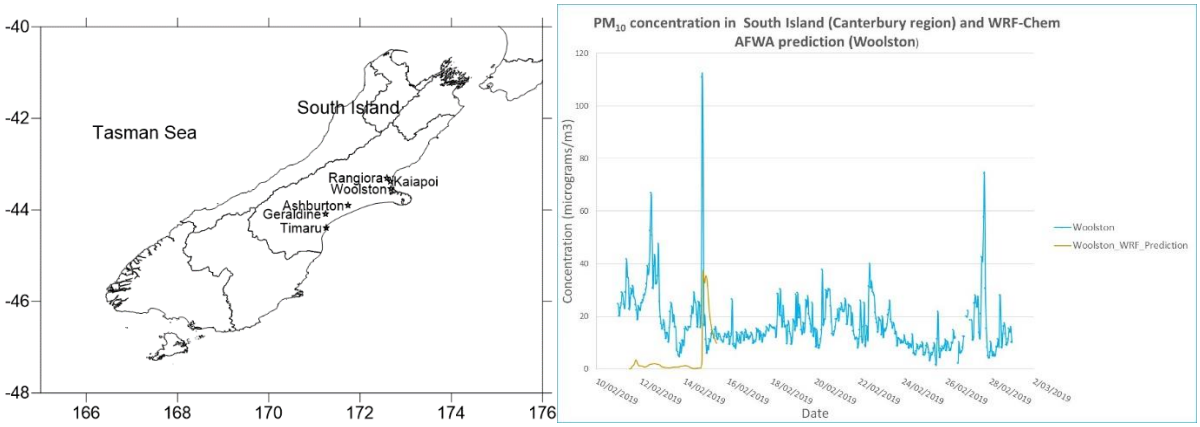

(a) (b)

Preprints (www.preprints.org) | NOT PEER-REVIEWED | Posted: 27 October 2019 doi:10.20944/preprints201910.0304.v1

Peer-reviewed version available at Atmosphere 2019, 10, 653; doi:10.3390/atmos10110653

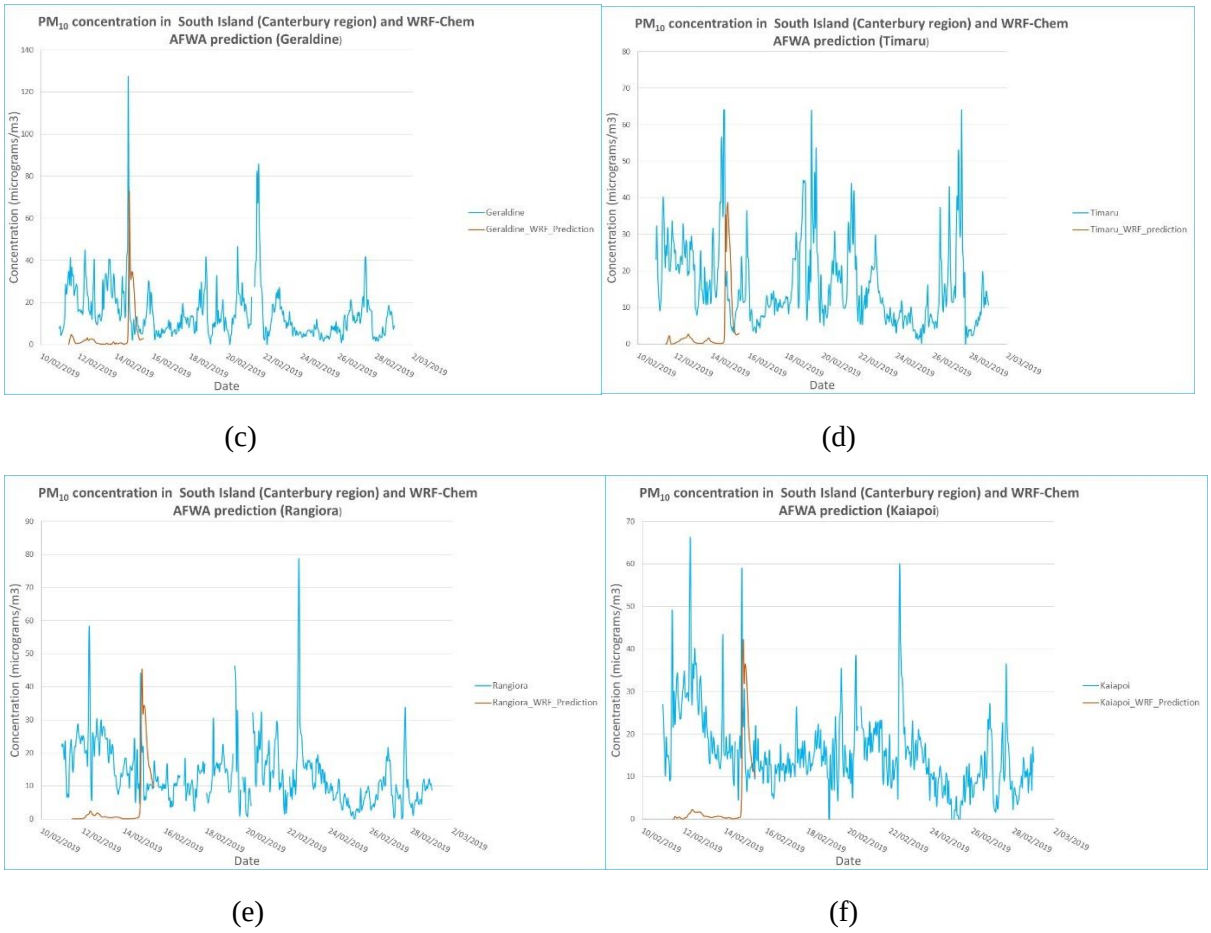

Figure 10 – (a) Monitoring stations in the Canterbury area of South Island, New Zealand for 14 February 2019. (b-f) Predicted PM_{10} from WRF-Chem with AFWA dust scheme (red line), FINN fire emission and MOZART and GOCART chemistry mechanism and observed PM_{10} (blue line) at Woolston, Geraldine, Timaru, Rangiora and Kaiapoi

The timing of predicted PM_{10} peaks coincide with the time of the corresponding peaks at the monitoring sites which are about 100km apart. Maximum PM_{10} concentrations, occurred at Woolston of 127 $\mu g/m^3$ (14 February 2019 08:00 UTC), 110 $\mu g/m^3$ (14/2/2019 05:00 UTC) Geraldine, 64 $\mu g/m^3$ (14/2/2019 05:00 UTC) Timaru, 59 $\mu g/m^3$ (14 February 2019 08:00 UTC) Kaiapoi and 44 $\mu g/m^3$ (14 February 2019 08:00 UTC) at Rangiora. The average daily PM_{10} concentration at these sites are about 20 $\mu g/m^3$. The maximum PM_{10} concentrations however are underpredicted by WRF-Chem MOZART/GOCART chemistry. The GOCART AFWA dust model in WRF-Chem is also highly varying depending on the value of the constants reflecting the local terrain conditions. Tuneable constants for dust emission in WRF-Chem with dust option can be chosen so that the PM_{10} prediction at the site is comparable with the observed data at the site. In Figure 10, the constant C_{mb} is set at 7.0 rather than 2.61 as specified in the original equation (8).

HYSPLIT forward trajectories of dust from the source area using HYSPLIT matrix forward analysis, as shown in Figure 11 for trajectories starting from 11 February 2019 4:00 UTC, indicate that the dust was transported along two paths: the North East dust path and the Eastern dust path. The pattern of trajectories is similar when the starting time of release from sources is between 10 February 2019 06:00 to 11 February 2019 22:00 UTC.

The source area is bounded by the rectangular area with lower left coordinate of (135°, -32°) and upper right coordinate of (145°, -28°) and each dust point source is at 50m AGL (above ground level) separated by 0.5° (resolution) in latitude and longitude. This area encompasses known dust sources (Lake Eyre,

Preprints (www.preprints.org) | NOT PEER-REVIEWED | Posted: 27 October 2019 doi:10.20944/preprints201910.0304.v1

Peer-reviewed version available at Atmosphere 2019, 10, 653; doi:10.3390/atmos10110653

South Simpson Desert, South Strzelecki Desert, Lakes Torrens and Gairdner region). The North East dust path carried dust from the northern part of Lake Eyre Basin (above latitude -30°) to Queensland and Great Barrier Reef off the coast while the Eastern dust path transports dust from southern part of Lake Eyre Basin and Lakes Torrens and Gairdner region to the Tasman Sea, New Zealand and Antarctica.

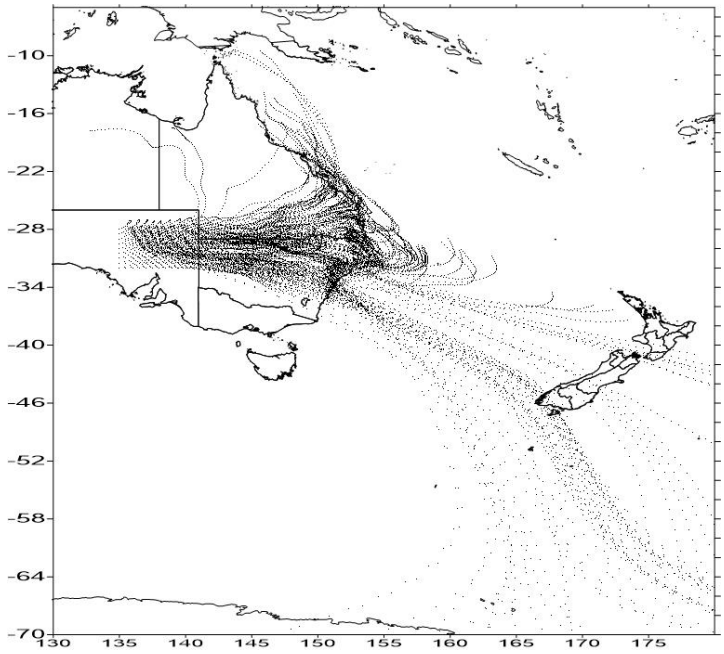

Figure 11 – HYSPLIT forward trajectory ensemble analysis for 96 hours at 10m height from a source area in Central Australia on 11 February 2019 4 UTC.

CALIOP lidar onboard CALIPSO satellite providing vertical structure of backscatter and aerosol types on the 14 February 2019 near the west coast of South Island in New Zealand shows dusty marine and dust layers above ground. High above the fresh marine aerosol layers are dust, polluted dust and dusty marine layers. There are also thick smoke aerosol layers present in the lidar measurement (black in Figure 12b).

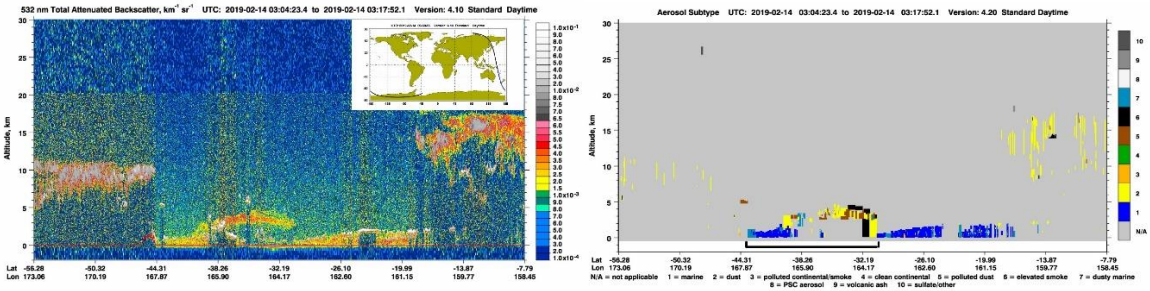

(a) (b)

Preprints (www.preprints.org) | NOT PEER-REVIEWED | Posted: 27 October 2019 doi:10.20944/preprints201910.0304.v1

Peer-reviewed version available at Atmosphere 2019, 10, 653; doi:10.3390/atmos10110653

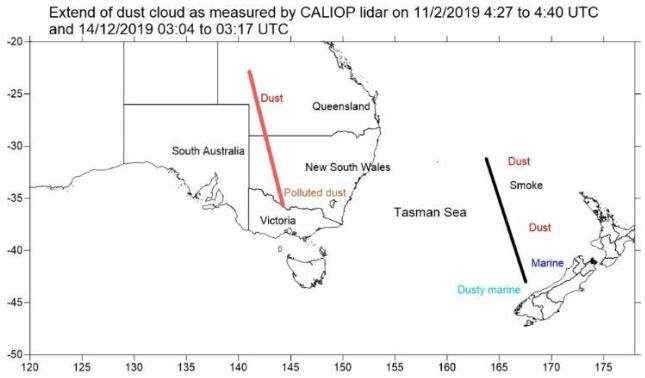

(c)

Figure 12 - (a) Lidar 532nm total attenuated backscatter vertical structure from 14 February 2019 03:04 to 03:17 UTC with CALIPSO satellite path (inset) on above the Tasman Sea near New Zealand (b) Aerosol subtype vertical profile as derived from CALIOP measurements with dust as yellow and smoke as black(c) Extent of aerosol layer clouds as measured by CALIPSO satellite on 11 February 2019 (red line) and on 14 February 2019 (black line). The labels correspond to aerosol types at the location indicated.

As shown in Figure 13 (a)(b), CALIOP lidar on CALIPSO satellite, above the coast of eastern Australia on 13 February 2019, showed dust and smoke aerosols layers situated above the dusty marine and marine aerosols layers. The dust and smoke aerosols layers (from approximately 2km to 5km) above the dust-contaminated marine and fresh marine aerosols layers below (from above sea level up to 2km high) extend to about 1400 km long.

The pattern of dust and smoke from CALIPSO vertical profile on the 13/2/2019 from 15:01 to 15:15 UTC can be compared with WRF-Chem vertical pattern of prediction of PM_{10}, dust of different sizes and total Black Carbon (both hydrophilic and hydrophobic Black Carbon) along the satellite path on 13/2/2019 15:00 UTC. Black Carbon (BC) is mostly indicative of combustible source origins while PM_{10} is a combination of both sources.

Figure 13 (d) (e) and (f) show the transect of dust (bin size 4), total black carbon and PM_{10} along the same CALIPSO satellite path of the coast of eastern Australia as shown as blue line in Figure 13 (c). The WRF-Chem prediction of layer of concentration of total black carbon originated mostly from combustion source such as biomass burning was predicted at height approximate 4km above ground centred around -27.3º latitude and 155.3º longitude (Figure 13 e) corresponds to the observed smoke plume layer located above the similar location at approximately the same height from 4 to 5km (Figure 13 b). Similarly, the prediction of spatial vertical pattern of PM_{10} layer along the transect corresponds well with CALIOP aerosol measurement pattern as shown in Figure 13 b. As the predicted pattern of dust of bin size 4 (3.0-6.0µm) is much similar to that of PM_{10}. this indicates that PM_{10} is mostly consisting of dust with little contribution from fires.

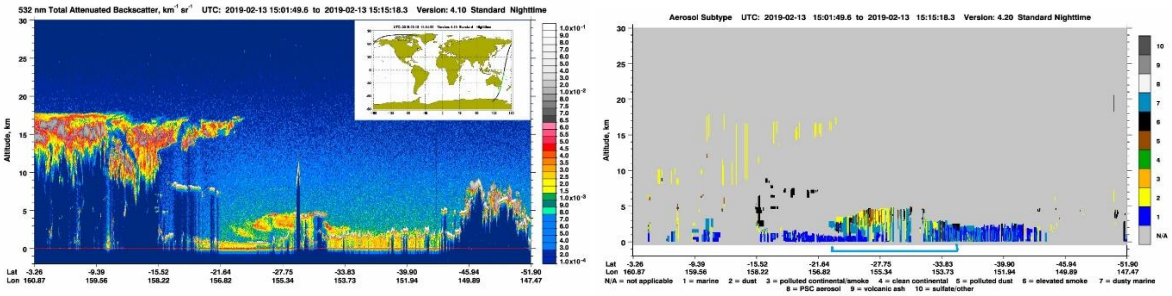

Preprints (www.preprints.org) | NOT PEER-REVIEWED | Posted: 27 October 2019 doi:10.20944/preprints201910.0304.v1

Peer-reviewed version available at Atmosphere 2019, 10, 653; doi:10.3390/atmos10110653

(a) (b)

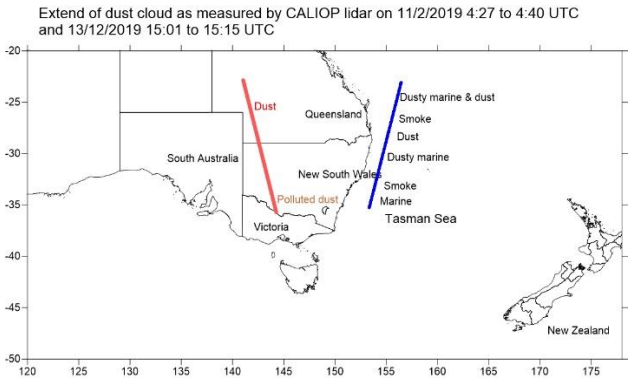

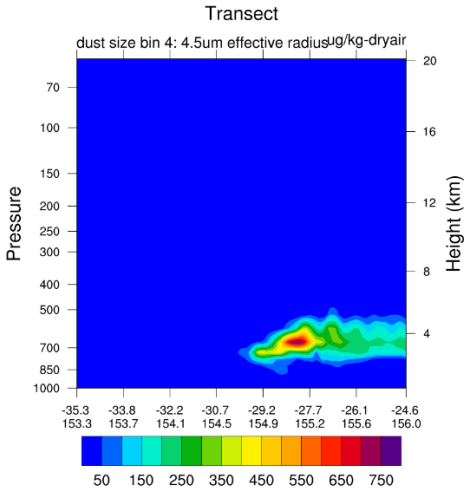

(c) (d)

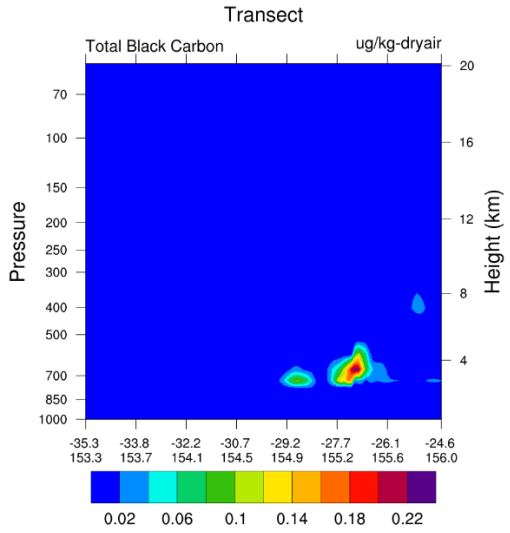

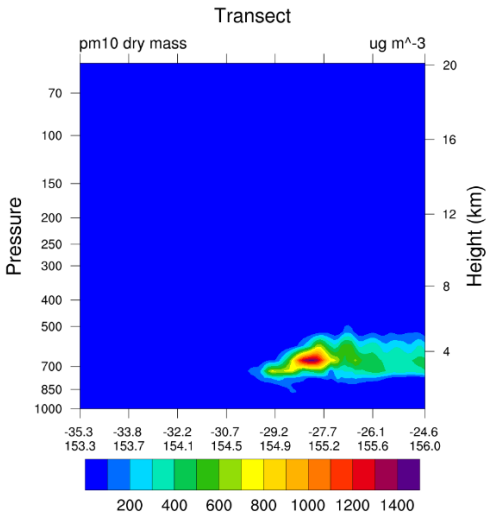

(e) (f)

Figure 13 - (a) Lidar 532nm total attenuated backscatter vertical structure from 13 February 2019 15:01 to 15:15 UTC with CALIPSO satellite path (inset) on 13 February 2019 above the coast of eastern Australia (b) Aerosol subtype vertical profile as derived from CALIOP measurements (c) Extent of dust clouds as measured by CALIPSO satellite on 11 February 2019 (red line) and on 13 February 2019 (blue line). The labels correspond to aerosol types at the location indicated. (d) (e) and (f) Transects of WRF-Chem predicted dust of size bin 4, total black carbon and PM_{10} on 13 February 2019 15:00 UTC along the same CALIPSO satellite path

3.2 Dust transport to Antarctica

Using HYSPLIT model, the forward trajectory analysis for 96 hours from the source area bounded by the rectangular area with lower left coordinate of (135°, -32°) and upper right coordinate of (145°, -28°) at 50m AGL shows that some of the dust trajectories not only reached New Zealand but also passed over Antarctica and beyond to the south Pacific Ocean east of the South America coast (off Chile).

Preprints (www.preprints.org) | NOT PEER-REVIEWED | Posted: 27 October 2019 doi:10.20944/preprints201910.0304.v1

Peer-reviewed version available at Atmosphere 2019, 10, 653; doi:10.3390/atmos10110653

Figure 14 shows the trajectories of transported dust from sources in Central Australia during the February 2019 dust storm.

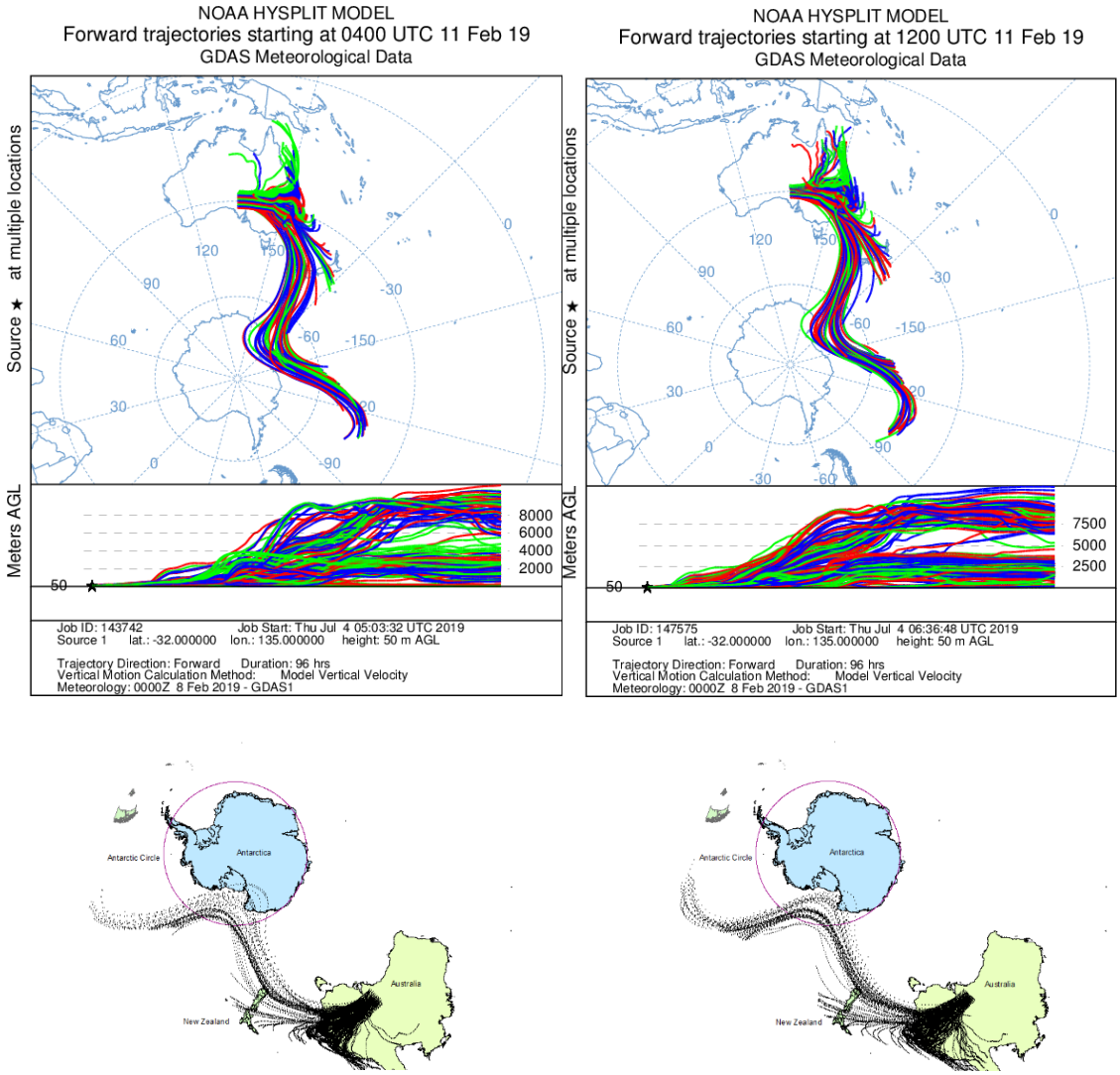

Figure 14 – (a) NOAA HYSPLIT model matrix forward trajectory analysis from dust source areas in Central Australia with particle release time at 11 February 2019 4:00 UTC (left) and 12:00 UTC (right) (b) Same as (a) but using ArcGIS to display selected trajectories.

Satellite observation is used to correlate with the forward trajectory analysis. On the 15 February 2019, the dust from the event that started on 13 February 2019 is passing through New Zealand and reaching the edge of Antarctica as detected by MODIS Terra/Aqua sensors. The CO emission from bushfires is still detected as CO column concentration of about 90ppb in the New England area of northern NSW (green colour in Figures 15 and 16)

Preprints (www.preprints.org) | NOT PEER-REVIEWED | Posted: 27 October 2019 doi:10.20944/preprints201910.0304.v1

Peer-reviewed version available at Atmosphere 2019, 10, 653; doi:10.3390/atmos10110653

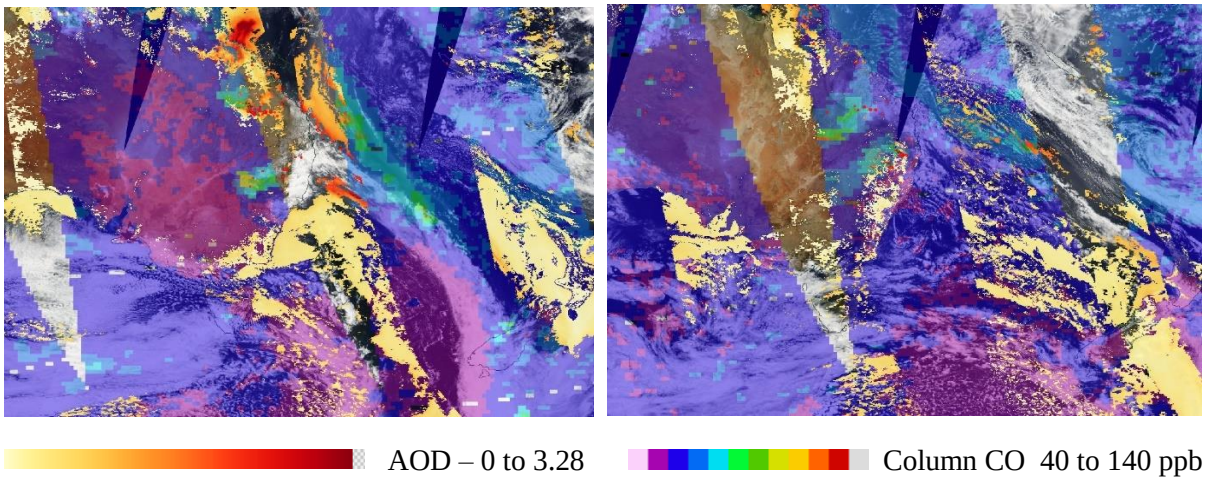

Figure 15 – AOD (yellow and red) and CO column concentration Aqua/Airs (pink and green) over the Tasman sea as revealed by MODIS on 14 February 2019 (left) and 15 February 2019 (right).

Figure 16 show the AOD from Aqua/Modis 3km land and ocean for dust and smoke particles and carbon monoxide (CO) from Aqua/Airs due to biomass fires from 13 February 2019 to 14 February 2019. They show the progress of the dust plumes and that New Zealand (both North and South Island) is slightly affected by dust (yellow and red). The dust column plume is then veering to Antarctica.

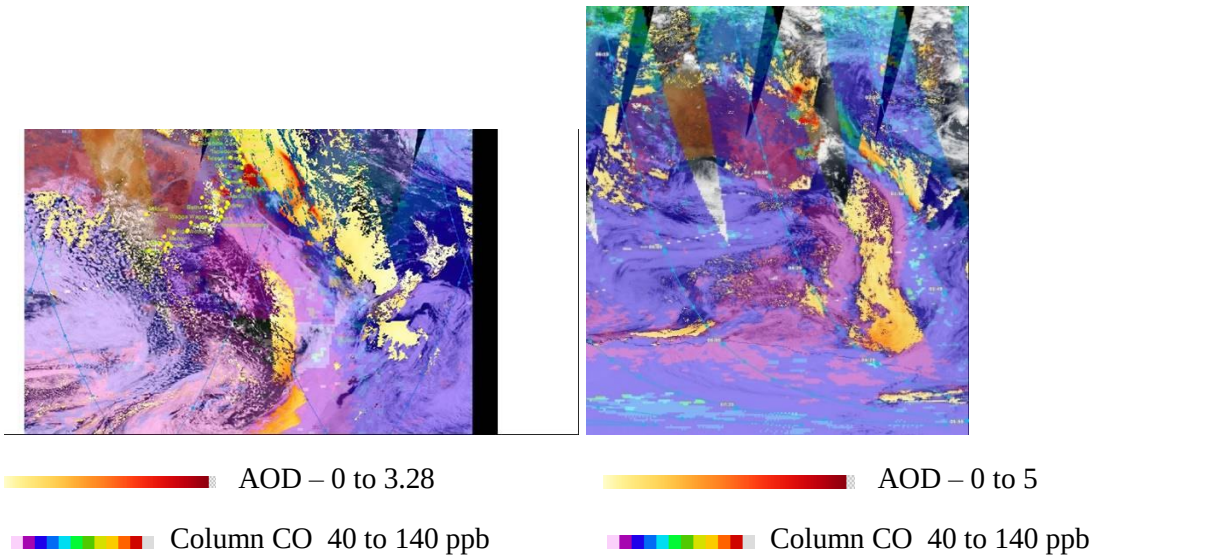

Figure 16 – The AOD Aqua/Modis and CO column Aqua/Airs daytime concentration on 13 February 2019 and location of towns and cities in the eastern seaboard of Australia (a) and AOD Terra/Modis and CO column Aqua/Airs daytime on 14 February 2019 (b). The pinkish and greenish colours are CO (carbon monoxide) column concentration.

The overall extent of AOD and daily AOD average over the region of Australia, New Zealand and Antarctica for the 13 and 14 February 2019 are shown in Figure A4 of the Appendix. The AOD over Antarctica is due to a number of different aerosol types: marine aerosols, dust and fire emission aerosols. CALIOP lidar data is used in helping to resolve the origin of AOD above Antarctica. Figure 17 shows the CALIOP lidar vertical structure of backscatter and aerosol type as measured by CALIPSO satellite on 15/12/2019.

Preprints (www.preprints.org) | NOT PEER-REVIEWED | Posted: 27 October 2019 doi:10.20944/preprints201910.0304.v1

Peer-reviewed version available at Atmosphere 2019, 10, 653; doi:10.3390/atmos10110653

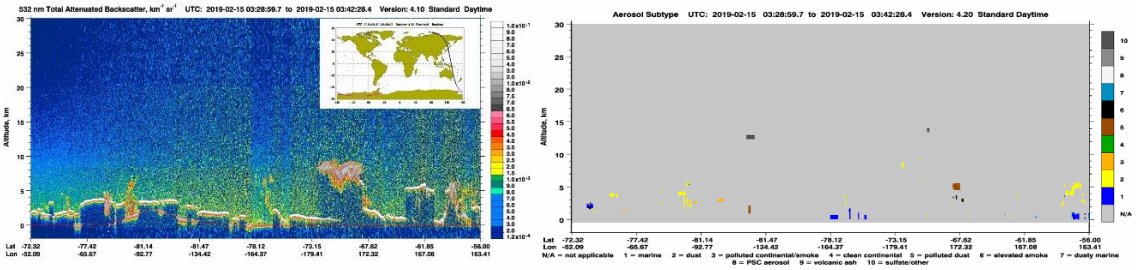

(a) (b)

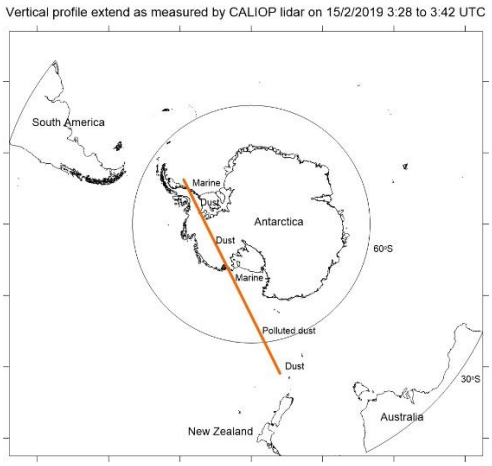

Figure 17 - (a) Lidar 532nm total attenuated backscatter vertical structure from 15 February 2019 03:42 to 03:42 UTC with CALIPSO satellite path (inset) above Antarctica (b) Aerosol subtype vertical profile as derived from CALIOP measurements (c) Extent of vertical profile as measured by CALIPSO satellite on 14 February 2019 (red line). The labels correspond to aerosol types at the location indicated

It is clear from CALIOP lidar measurements that the aerosols above Antarctica are of dust origins (dust and polluted dust types) from 2km to 6km height with marine aerosols confined to layer 0 to 2km above ground. These high dust layers above Antarctica indicate long-range transport of dust from Australia. As for smoke particles due wild fires in northern NSW Australia, they were transported to the Tasman sea (at high latitude and altitude) and did not affect the ground concentration in South Island of New Zealand. However, scattered smoke layers at very high altitude (above 10km up to 15km) were detected as shown in Figure 17 above Antarctica and they could have their origins from large fires and biomass burnings in Australasian regions of Indonesia and northern Australia.

4. Discussion

Australia is a dry continent and wild fires occur in many parts of Australia mainly in northern Australia especially during the dry and hot period of summer. In addition, frequent dust storms, from deserts in central Australia and agricultural land where annual rainfall is below 500mm annual rainfall, can cause dust to be transported under favourable meteorological condition to the east coast and beyond to the Tasman sea, New Zealand and as far as Antarctica. This transport of dust along the south east dust pathway has been occurring for 350,000 years [14]. In glacial periods, dust transport increases. In three out of four cores analysed by Hesse 1994 [4], sediment accumulation rates have fallen since a peak 130,000 to180,000 years ago. De Deckker et al. 2010 [19] reported that while Australia is not currently in a glacial period, its environment has becoming increasingly dry over the last 6000 years.

Marx et al 2018 [11] reported that conversion of land to agriculture globally over the last 250 years has resulted in increased dust sources. Ginoux et al 2012 [40] estimated that 25% of global dust emission is from areas associated with anthropogenic activities, that is, like agriculture. In the case of eastern

Australia, dust sources are a mix of natural and anthropogenic sources. Natural sources in central Australia like dry lakes and floodplains are driven by El Niño–Southern Oscillation (ENSO) [51]. During wet La Nina years, sediment is transported to the topographically low areas of Central Australia. During the El Nino dry years, the dust is emitted and transported. Marx et al 2018 [11] also reported that dust concentration at Hokitika, South Island, New Zealand has increased between 1991 and 2001 and with the current Southern Oscillation Index (SOI) being mostly negative since 2014 (their Fig 9), this is also contributing to the current dust transport. Prior to 1991, they report dust deposition in the Australian Snowy Mountains was about three times higher than post 1990 (their Fig 23).

Brahney et al. 2019 [52] in their study of dust deposition to two alpine lakes in Kahurangi National Park, South Island of New Zealand, using geochemical proxies have found that dust deposition began to increase around 1900, with the greatest deposition rates occurring from ~1920 to ~1990 and appear to have declined in subsequent decades. This change in dust deposition in New Zealand lakes is consistent with dust records from the Antarctic Ice Sheet and Eastern Australia. They found that this temporal change in dust deposition rate follows the temporal pattern of land use in south and central Australia during the twentieth century. And they suggest that land clearing and agricultural practices causing an increase in soil erosion significantly especially in the early 20th century is the cause of increased dust deposition in New Zealand lakes.

This study shows that dust is also transported to Antarctica as did De Deckker et al. 2010 [19] who reported an event starting 1 April 2008 in central and south eastern Australia travelled over the next 11 days to Antarctica. This process has been going on for thousands of years. Dust in ice cores dating back to 170,000 years showed evidence of dust transported from south eastern Australian continent [19].

O'Loingsigh et al. 2017 [17] showed that the Eastern dust pathway transport of dust to the coast from sources in central Australia, as described in their study, is associated with dust export to New Zealand and dust deposition over the Tasman Sea. In our study, the dust event of February 2019 followed the eastern pathway to the coast and our results confirm that dust from this event indeed crossed over the Tasman Sea and reached New Zealand and beyond including Antarctica. The long-range transport of dust from desert and dry plains in central Australia and western New South Wales to the Tasman Sea and beyond is also made possible due to the uplifting of the dust cloud after crossing the elevated Great Dividing Range which is about 3700km long roughly paralleling the east coast of Australia extending from Cape York peninsular in Queensland to New South Wales and Victoria. In New South Wales, the average height of the highland is about 1000m and rising to peak of 2228m at Mount Kosciuszko in the Australian Alps near the New South Wales-Victoria border. Xu et al. 2018 [53] in their study of global dust transport from the Tibetan Plateau (TP) have found upper troposphere (above ~8km) dust load and downstream dust flux are significantly higher relative to those over other major dust sources of the Northern Hemisphere. This enables the long-range transport of dust around the Northern Hemisphere as the TP acts as a channel for transporting dust from the lower atmosphere to the upper troposphere. The Great Dividing Range is not that high as the TP but the uplifting role is similar.

Ginoux et al 2004 [6] estimated from their modelling study on global distribution of aeolian dust from 1981 to 1996 with the Global Ozone Chemistry Aerosol Radiation and Transport (GOCART) model that the North African deserts (Sahara and Sahel) contribute about 65% of the global emissions of dust. Compared to other regions, Australia annual average budget of dust emission (from 1981 to 1996) is 61 Tg year^{-1} which is less than North Africa (1430), Asia (496) but higher than South America (49), South Africa (22) and North America (9). North Africa dust sources also contribute to about half of the dust aerosols to the world oceans [23], mainly to the Atlantic Ocean. Australian dust storms from Central Australia deserts are mostly deposited to the Southern Ocean and Tasman Sea. In this study, dust from the 11-15 February 2019 event is shown to be transported by prevalent south westerly from the emissive dust sources in the centre of Australia to the east coast and then north easterly to the

Tasman Sea. After encountering easterly wind, dust was then transported southward reaching New Zealand and Antarctica.

Compared to other studies of dust transport in the northern hemisphere, such as in Asia where the long range dust transport from Taklimakan and Gobi deserts is usually following the eastward paths by prevailing midlatitude westerlies across China, reaching Korean Peninsula, Japan and occasionally transported across the Pacific to North America [54]. The dust transport from Central Australia desert and arid region also follow the eastward patterns by prevailing south westerlies or westerlies toward the Tasman Sea, New Zealand and beyond, occasionally to Antarctica. Based on MISR (Multiangle Imaging Spectroradiometer) and HYSPLIT forward trajectory analysis, Yu et al. 2019 [54] studied the trans-Pacific dust transport from Asian deserts to North America and found that Taklimakan dust dominantly affecting south of 50°N in North America while Gobi dust primarily affect north of 50°N. Zhang, Tong et al. 2016 [55] in their study of dust source identification in East Asia from 2010-2015 using MODIS data and HYSPLIT trajectory analysis have shown that dust from central Asian deserts such as Taklimakan Desert and Gobi Desert can be transported northwards by the Mongolia Cyclone to the Far East region and even the Arctic Circle.

Li et al. 2008 [56] studied the distribution, transport and deposition of dust in the Southern Ocean and Antarctica from dust sources in South America, Australia and Northern Hemisphere using GFDL Atmospheric General Circulation Model AM2 for a 20-year period (1999-1998). They found that the majority of dust transported to the Southern Ocean came from Australia (120 Tg/year) then Patagonia in South America (38 Tg/year) and inter-hemispheric transport from Northern Hemisphere (31 Tg/year). A small fraction of these are deposited in the Southern Ocean and Antarctica (7 Tg/year). Our study of the February 2019 dust storm in eastern Australia shows that dust from this event has been transported to Antarctica.

As Yu et al. 2019 [54] noted that using tracer mode in trajectory Lagrangian modelling analysis such as HYSPLIT, gravitational settling and wet deposition processes are ignored, therefore the long-range transport of dust is usually overestimated compared to the actual range. In this study, we primarily used Eulerian dispersion WRF-Chem model which takes into account the wet and dry deposition but Lagrangian HYSPLIT was also used to illustrate the ensemble pathways of dust trajectories as likely dust transport routes to complement and support the understanding of dispersion process in WRF-Chem prediction.

As for the dust model in the WRF-Chem model, there is limit in the current WRF-Chem dust schemes based on topographic soil erodibility which is confined mostly in the central Australian arid region. Rather than static, erodibility defined as soil erosion efficiency under given meteorological forcing (i.e wind speed), soil erodibility is dynamically changed depending on local environmental condition such as land use, land cover type, soil moisture [57]. In our study, soil moisture is provided by WRF-Chem meteorological component. Observation and satellite data such as MODIS have been used to calibrate this dynamic erodibility in the dust source region. But land use and land cover (or green fraction) is based on static maps. Agricultural areas, such as the western Riverina and Mallee regions in the border area of New South Wales and Victoria, are not properly accounted for in the topographic soil erodibility map. The Riverina and Mallee regions have also been identified as dust sources [17] [58] [59] used the rainfall data from the Australian Bureau of Meteorology (BOM) and land cover data derived from MODIS data to account for seasonal changes in soil erodibility and dust emission to study the dust climatology for a ten-year period for western New South Wales (NSW), Australia.

Similarly, Ginoux et al. 2012 [40] used 0.1° x 0.1° gridded satellite data MODIS Deep Blue (MODIS DB) Level 2 from 2003 to 2009 to detect and attribute natural and anthropogenic dust sources for different seasons. The inclusion of anthropogenic activities such as land clearing, agricultural activities and grazing and ephemeral stream, lakes and rivers in arid region (such as Lake Eyre Basin in Australia) allowed them to assess anthropogenic and hydrologic impacts on dust emission at the global scale. The

largest source with the highest annual frequency over Australia continent is in channel country, especially at the mouth of the Warburton River feeding North Lake Eyre. Some of the lakes in Lake Eyre Basin are active dust source all year long while others are active for one or two seasons or not active for all seasons. The inclusion of MODIS data to improve the dust source function (Equation 2) by detecting more hot spots or sources can result in better prediction of dust concentration and deposition in our study. But in applying the new Ginoux source function in West Asia, Nabavi et al. 2017 [43] found that it did not provide a significant improvement in the accuracy of WRF-Chem predictions.

The use of satellite data can result in false identification of dust sources where persistent or seasonal long-range transport and deposition of dust or biomass burning occur. To eliminate this false identification, Parajuli et al., 2014 [57] used the correlation between MODIS Deep Blue AOD and wind speed as a proxy for erodibility over an area. Erodibility as the maximum correlation of AOD and wind speed during the driest season is used and any correlation below this maximum reflects variation in environment condition such as soil moisture, vegetation cover. The use of such dynamic erodibility proxy can improve the prediction of dust concentration and AOD in the current dust scheme in WRF-Chem model.

In our current study for the dust event of February 2019, the dust emission was mostly confined to the Lake Eyre Basin and dust was transported across New South Wales to the east coast of Australia. Other Australian studies [51] [60] [61] [62] highlighted the importance of Central Australia as a dust source area. Zhang et al. 2016 [55] in their study of identification of dust sources and hotspots in East Asia during 2000-2015 period by analysing more than 2000 MODIS images of dust storm events and HYSPLIT back trajectory analysis have found that the dominant dust sources are sandy lands and lake beds, rather than the sandy and stone deserts with increased frequencies in summer and autumn. Lake Eyre Basin whose ephemeral lakes and streams are fed with flood water from Queensland was identified by Ginoux et al. 2012 as the source of most dust storms in east Australia during the dry and drought period.

Zhang et al. 2016 [55] also showed that changes in land use associated with anthropogenic activities such as mining and excessive exploitation of water resources are one of the major factors leading to an expansion of dust source regions, especially for the northeastern part of Taklimakan desert.

Our future study of dust transports of dust storm events from Central and Eastern Australia will make use of seasonal soil erodibility map derived from satellite data in WRF-Chem to improve the prediction of dust transport and concentration over the modelling domain. This erodibility map will include the Riverina-Mallee region as a significant dust source. The results of such study can then be compared with the current Ginoux dust source function to determine whether the new Ginoux source function is better in dust prediction.

Anisimov et al. 2018 [63], in their study of haboob (desert dust storm) over the Arabian Peninsula, using WRF-Chem 3.7.1 with GOCART dust emission scheme and MOSAIC aerosol chemistry, have found that WRF-Chem underestimated the PM_{10} mass concentration by nearly a factor of 2. They suggested that the current dust GOCART parameterization of the size distribution of the emitted dust, underestimate the number of large particles at strong wind conditions. Does et al 2018 [24] have found that even giant particles (>75 µm) were transported long-range from Sahara Desert to the Atlantic Ocean.

In our study using WRF-Chem GOCART-AFWA emission dust scheme, we also find that the predicted PM_{10} using the original constant C_{mb}=2.61 in the horizontal saltation flux equation instead of 1 from Marticorena and Bergametti 1995 [46] as implemented in WRF-Chem still underpredicted the PM_{10}. When this tunable constant is increased to 7, the result is better matched with observation. Eltahan et al. 2018 [31] has found that tunable constant C_{mb}=6 resulted in AOD prediction having better match

with AOD as measured by AERONET network over Cairo during the 31 March 2013 dust storm in Egypt.

5. Conclusion

In this study, we have conducted simulation of dust emission and wildfire smoke transport from Australia to the Tasman Sea, New Zealand and beyond to Antarctica during 11 to 15 February 2019. Such long-range transport and deposition of dust has been occurring for hundreds thousands of years as evidenced by the detection of dust in deep sea sediment cores in the Tasman Sea and ice cores in New Zealand and Antarctica. The 11 to 15 February 2019 event sits within the context of being lower than previous glacial periods, lower than the 1900 to 1990 period, but increasing dust emission since 1991 [11]. The current increase over the last 30 years is a function of a series of dry periods.

The simulation using WRF-Chem and observed data on ground and satellites show that long range transport of dust has affected air quality, not only in the eastern seaboard of Australia, but also across the Tasman Sea in South Island of New Zealand as detected by monitoring stations in the Canterbury region. This is due to the intrusion of long range transported dust layer from above to ground level.

In northern NSW, there were wild fires during this period. Simulation of both dust and wild fires emission in WRF-Chem and observation data from CALIOP lidar showed that aerosols of both sources were carried to the Tasman sea, but the aerosol clouds contained more dust aerosols than aerosols from biomass burnings.

There is evidence of dust transport at high altitude to Antarctica as measured by MODIS satellite AOD and CALIPSO aerosol vertical structure from CALIOP lidar above Antarctica from the storm in Australia on 11-15 February period. The transport of dust from Australia to New Zealand and beyond are also due to the current drought in eastern Australia. It continues a pattern that has occurred for thousands of years as reported in many previous studies including studies of lake-sediment and ice core data from New Zealand and Antarctica.

This study of the dust storm in February 2019 contributes to the understanding of dispersion and long-range transport of dust from this event and confirm that dust following the eastern pathway from central Australia to the coast can reach New Zealand and Antarctica.

Author Contributions: Conceptualization, H.N., M.R., J.L.; methodology, H.N., J.L.; data procurement: H.N, D.S, J.L.; formal analysis, H.N.; investigation, H.N., J.L.; writing—original draft preparation, H.N., J.L.; writing, H.N., J.L.; visualization, H.N.; supervision, H.N., M.R.; project administration, M.R.

Funding: This research received no external funding.

Acknowledgements: Analyses and visualizations, where they are indicated in the paper, were produced with the Giovanni online data system, developed and maintained by the NASA GES DISC, and CALIPSO satellite products from NASA Langley Research Centre. We also acknowledge the NOAA Air Resources Laboratory (ARL) for the provision of the HYSPLIT transport and dispersion model and/or READY website (http://www.ready.noaa.gov) used in this publication.

Conflicts of Interest: The authors declare no conflict of interest

References

1. Rotstayn L, Keywood A., Forgan B., Gabric A., Galbally I., Gras J., Luhar M., McTainsh G., Mitchell R., Young S., 2009. Possible impacts of anthropogenic and natural aerosols on Australian climate and weather: a review, *International Journal of Climatology* 29: 461-479. DOI: 10.1002/joc.1729

2. Leys J., Heidenreich S., Strong C., McTainsh G., Quigley S., 2011. PM_{10} concentrations and mass transport during "Red Dawn" - Sydney 23 September 2009. *Aeolian Research* 3: 327-342

3. Knight A., McTainsh G., Simpson R., 1995. Sediment loads in an Australian dust storm: implications for present and past dust processes. *Catena* 24: 195-213

4. McTainsh G., Chan Y., McGowan H., Leys J., Tews K., 2005. The 23rd October 2002 dust storm in eastern Australia: characteristics and meteorological conditions. *Atmospheric Environment* 39: 1227-1236.

5. Chan Y., McTainsh G., Leys J., McGowan H., Tews E.. 2005. Influence of the 23 October 2002 dust storm on the air quality of four Australian cities. *Water, Air and Soil Pollution* 164: 329-348

6. Ginoux, P., Prospero, J., Torres, O., Chin, M., 2004, Long-term simulation of global dust distribution with the GOCART model: correlation with North Atlantic Oscillation, *Environmental Modelling & Software* 19:113–128.

7. Shao, Y., Wyrwoll, K-H, Chappell, A., et al., 2011, Dust cycle: An emerging core theme in Earth system science, *Aeolian Research* 2 (2011) 181–204.

8. Bowler J., 1976. Aridity in Australia: Age, origins and expression in aeolian landforms and sediments. *Earth-Science Reviews* 12: 279-310

9. Sprigg R. 1982. Alternating wind cycles of the Quaternary era, and their influence on aeolian sedimentation in and around the dune deserts of south eastern Australia. In *Proceedings INQUA Loess Commission Workshop: Quaternary Dust Mantles of China, New Zealand and Australia*.

10. O'Loingsigh, T., Chubb, T., Baddock, M., et al., 2017, Sources and pathways of dust during the Australian "Millennium Drought" decade, *J. Geophys. Res. Atmos.*, 122, 1246–1260, doi:10.1002/2016JD025737

11. Marx S., Kamber B., McGowan H., Petherick L., et al., 2018, Palaeo-dust records: A window to understanding past environments. *Global and Planetary Change* 165: 13-43. DOI: 10.1016/j.gloplacha.2018.03.001

12. Gabric A., Cropp R, McTainsh G, Butler H, Johnston B., O'Loingsigh T., Van Tran D. 2016. Tasman Sea biological response to dust storm events during the austral spring of 2009. *Marine and Freshwater Research* 67: 1090-1102. DOI: 10.1071/MF14321

13. Hesse P., 1993. Aeolian dust in Quaternary Tasman Sea sediments. *Quaternary Australia* 11: 43

14. Hesse P., 1994. The record of continental dust from Australia in Tasman Sea sediments., *Quaternary Science Reviews* 13: 157-272

15. Marx S., Kamber B., McGowan H.. 2005, Provenance of long-travelled dust determined with ultra-trace-element composition: a pilot study with samples from New Zealand glaciers. *Earth Surface Processes and Landforms* 30: 699-716. DOI: 10.1002/esp.1169

16. Marx S., Kamber B., McGowan H., 2008, Scavenging of atmospheric trace metal pollutants by mineral dusts: Inter-regional transport of Australian trace metal pollution to New Zealand. *Atmospheric Environment* 42: 2460-2478. DOI: 10.1016/j.atmosenv.2007.12.014

17. McGowan H., McTainsh G., Zawar-Reza P., Sturman A., 2000. Identifying regional dust transport pathways: Application of kinematic trajectory modelling to a trans-Tasman case. *Earth Surface Processes and Landforms* 25: 633-647

18. McGowan H., Kamber B, McTainsh G., Marx S., 2005, High resolution provenancing of long travelled dust deposited on the Southern Alps, New Zealand. *Geomorphology* 69: 208-221. DOI: 10.1016/j.geomorph.2005.01.005

19. De Deckker, P., Norman, M., Goodwin, I., et al., 2010, Lead isotopic evidence for an Australian source of aeolian dust to Antarctica at times over the last 170,000 years, *Palaeogeography, Palaeoclimatology, Palaeoecology*, 285:205–223, DOI: 10.1016/j.palaeo.2009.11.013

20. Revel-Rolland, M, De Deckker, P., Delmonte, B. et al., 2006, Eastern Australia: A possible source of dust in East Antarctica interglacial ice, *Earth and Planetary Science Letters*, 249:1–13

21. Calvo E., Pelejero C., Logan G., De Deckker P., 2004. Dust-induced changes in phytoplankton composition in the Tasman Sea during the last four glacial cycles. *Paleoceanography* 19: 10.1029/2003PA000992. DOI: 10.1029/2003PA000992

22. Shaw E., Gabric A., McTainsh G., 2008. Impacts of aeolian dust deposition on phytoplankton dynamics in Queensland coastal waters. *Marine and Freshwater Research* 59: 951-962. DOI: 10.1071/MF08087

23. Does, M., Korte, L., Munday, C., Brummer, G. et al., 2016, Particle size traces modern Saharan dust transport and deposition across the equatorial North Atlantic. *Atmospheric Chemistry and Physics*. 16. 13697-13710. 10.5194/acp-16-13697-2016.

24. Does, M., Knippertz , P., Zschenderlein , P., et al., 2018, The mysterious long-range transport of giant mineral dust particles, *Science Advances*, Vol. 4, no. 12, eaau2768, DOI: 10.1126/sciadv.aau2768

25. Chen, S., Huang, J, Kang, L., et al., 2016, Emission, transport and radiative effects of mineral dust from Taklimakan and Gobi Deserts: comparison of measurements and model results, *Atmos. Chem. Phys. Discuss*, 17(1-3), doi:10.5194/acp-2016-531

26. Chen, S., Lu, C., McQueen, J. Lee, P., 2018, Application of satellite observations in conjunction with aerosol reanalysis to characterize long-range transport of African and Asian dust on air quality in the contiguous U.S., *Atmospheric Environment*, 187 174–195.

27. Cavazos-Guerra, C., Todd, M., 2012, Model Simulations of Complex Dust Emissions over the Sahara during the West African Monsoon Onset, *Advances in Meteorology*, doi:10.1155/2012/351731

28. Chen, S., Zhao, C., Qian, Y., et al., 2014, Regional modeling of dust mass balance and radiative forcing over East Asia using WRF-Chem, *Aeolian Research*, http://dx.doi.org/10.1016/j.aeolia.2014.02.001

29. Fountoukis, C., Ackermann, L., Ayoub, M.A. et al., 2016, Impact of atmospheric dust emission schemes on dust production and concentration over the Arabian Peninsula, *Model. Earth Syst. Environ.* 2: 115. https://doi.org/10.1007/s40808-016-0181-z

30. Rizza, U., Bernaba, F., Miglietta, M., et al, 2017, WRF-Chem model simulations of a dust outbreak over the central Mediterranean and comparison with multi-sensor desert dust observations, *Atmospheric Chemistry and Physics* 17(1):93, DOI: 10.5194/acp-17-93-2017.

31. Eltahan, M., Shokr , M., Sherif , A., 2018, Simulation of Severe Dust Events over Egypt Using Tuned Dust Schemes in Weather Research Forecast (WRF-Chem), *Atmosphere*, 9, 246; doi:10.3390/atmos9070246

32. Chen, S., Yan, T., Zhang, X., et al., 2018, Dust modeling over East Asia during the summer of 2010 using the WRF-Chem model, *J. of Quantitative Spectroscopy and Radiative Transfer*, 213:1-12

33. Yuan, T., Chen, S., Huang, J., et al., 2019, Sensitivity of simulating a dust storm over Central Asia to different dust schemes using the WRF-Chem model, *Atmospheric Environment*, 207:16-29, https://doi.org/10.1016/j.atmosenv.2019.03.014

34. Shao, Y., 2001, A model for mineral dust emission, *J. of Geophysical Research*, 106:20239-20254, https://doi.org/10.1029/2001JD900171

35. Shao, Y., 2004, Simplification of a dust emission scheme and comparison with data, *J. of Geophysical Research*, 109, D10202, doi:10.1029/2003JD004372

36. Shao, Y., Ishizuka, M., Mikami, M, Leys, J., 2011, Parameterization of size-resolved dust emission and validation with measurements. *J. Geophysical Research*, 116, D08203, doi:10.1029/2010JD014527

37. Su, L., Fung, J., 2015, Sensitivities of WRF-Chem to dust emission schemes and land surface properties in simulating dust cycles during springtime over East Asia, *Journal of Geophysical Research: Atmospheres*, https://doi.org/10.1002/2015JD02344

38. Flaounas, E., Kotroni, V., Lagouvardos, K., et al., 2017, Sensitivity of the WRF-Chem (V3.6.1) model to different dust emission parametrisation: assessment in the broader Mediterranean region, *Geosci. Model Dev.*, 10, 2925–2945, 2017, https://doi.org/10.5194/gmd-10-2925-2017

39. Ma, S., Zhang, X., Gao, C., et al. 2019, Multi-model simulations of springtime dust storms in East Asia: Implications of an evaluation of four commonly used air quality models (CMAQ v5.2.1, CAMx v6.50, CHIMERE v2017r4, andWRF-Chem v3.9.1), *Geosci. Model Dev. Discuss.*, https://doi.org/10.5194/gmd-2019-57.

40. Ginoux, P., Prospero, J., Gill, et al., 2012, Global-scale attribution of anthropogenic and natural dust sources and their emission rates based on MODIS Deep Blue aerosol products, *Rev. Geophys.*, 50, RG3005, doi:10.1029/2012RG000388.

41. Ginoux, P., Chin, M., Tegen, I., et al., 2001, Sources and distributions of dust aerosols simulated with the GOCART model, *J. Geophys. Res.-Atmos.*, 106: 20255-20273

42. LeGrand, S., Polashenski, C., Letcher, T., et al., 2019, The AFWA dust emission scheme for the GOCART aerosol model in WRF-Chem v3.8.1, *Geosci. Model Dev.*, 12, 131–166, https://doi.org/10.5194/gmd-12-131-2019

43. Nabavi, S., Haimberger, L., Samimi, C., 2017, Sensitivity of WRF-chem predictions to dust source function specification in West Asia, *Aeolian Research*, 24 (2017) 115–131

44. Office of Environment and Heritage, NSW, 2019, DustWatch Report February 2019, https://www.environment.nsw.gov.au/-/media/OEH/Corporate-Site/Documents/Land-and-soil/dustwatch-report-february-2019-190002.pdf

45. Guerschman, J., Scarth, P., Mcvicar, T., et al., 2015, Assessing the effects of site heterogeneity and soil properties when unmixing photosynthetic vegetation, non-photosynthetic vegetation and bare soil fractions from Landsat and MODIS data, *Remote Sensing of Environment* 161, DOI: 10.1016/j.rse.2015.01.021

46. Marticorena, B., Bergametti, G., 1995, Modeling the atmospheric dust cycle. Part 1: Design of a soil-derived dust emission scheme, *J. of Geophysical Research Atmospheres* 100(D8):16415-16430, DOI: 10.1029/95JD00690

47. Zhao, C., Liu, X., Leung, R., et al. 2010, The spatial distribution of mineral dust and its shortwave radiative forcing over North Africa: Modeling sensitivities to dust emissions and aerosol size treatments, *Atmospheric Chemistry and Physics*, DOI: 10.5194/acp-10-8821-2010.

48. Wang, L., Fu, J., Wei, W., et al., 2018, How aerosol direct effects influence the source contributions to $PM_{2.5}$ concentrations over Southern Hebei, China in severe winter haze episodes, *Frontiers of Environmental Science & Engineering* 12(3), DOI: 10.1007/s11783-018-1014-2

49. Zhao, C., Liu, X., Leung, L.R., Hagos, S., 2011. Radiative impact of mineral dust on monsoon precipitation variability over West Africa. *Atmos. Chem. Phys.* 11, 1879–1893. http://dx.doi.org/10.5194/acp-11-1879-2011.

50. Verruijt, A., 2001, Soil Mechanics Handbook, Delft University of Technology, Delft, The Netherlands, 2001.

51. Bullard J., McTainsh G. 2003. Aeolian-fluvial interactions in dryland environments: examples, concepts and Australia case study. *Progress in Physical Geography* 27: 359-389

52. Brahney, J., Ballantyne, A., Vandergoes , M., et al., 2019, Increased dust deposition in New Zealand related to 20th-century Australian land use, DOI: 10.1029/2018JG004627

53. Xu, C., Ma, Y., Yang, K et al., 2018, Tibetan Plateau Impacts on Global Dust Transport in the Upper Troposphere, *Journal of Climate*, 31:4745-4755, DOI: 10.1175/JCLI-D-17-0313.1

54. Yu, Y., Kalashnikova, O., Gary, M., et al., 2019, Climatology of Asian dust activation and transport potential based on MISR satellite observations and trajectory analysis, *Atmos. Chem. Phys.*, 19, 363–378, 2019, https://doi.org/10.5194/acp-19-363-2019

55. Zhang, X., Tong, D., Wu, G. et al., 2016, Identification of dust sources and hotspots in East Asia during 2000-2015: implications for numerical modeling and forecasting, *Atmospheric Chemistry and Physics Discussion*. 10.5194/acp-2016-681.

56. Li, F., Ginoux, P., Ramaswamy, V., 2008, Distribution, transport, and deposition of mineral dust in the Southern Ocean and Antarctica: Contribution of major sources, *J. of Geophysical Research*, 113, D10207, doi:10.1029/2007JD009190, 2008

57. Parajuli, S, Yang, Z., Kocurek, G., 2014, Mapping erodibility in dust source regions based on geomorphology, meteorology, and remote sensing, *J. Geophys. Res. Earth Surf.*, 119:1977–1994, doi:10.1002/2014JF003095

58. Bhattachan, A., D'Odorico, P., 2014, Can land use intensification in the Mallee, Australia increase the supply of soluble iron to the Southern Ocean? *Nature Sci. Rep.* 4, 6009; DOI:10.1038/srep06009.

59. Leys, J., Strong, C., Heindenreich, S., et al., 2018, Where She Blows! A Ten Year Dust Climatology of Western New South Wales Australia, *Geosciences (Switzerland)*, 8(7):232, DOI: 10.3390/geosciences8070232

60. Strong C., Parsons K., McTainsh G., Sheehan A., 2011, Dust transporting wind systems in the lower Lake Eyre Basin, Australia: A preliminary study. *Aeolian Research* 2: 205-214. DOI: 10.1016/j.aeolia.2010.11.001

61. O'Loingsigh T., McTainsh G., Tews E., Strong C., Leys J., Shinkfield P., Tapper N., 2014. The Dust Storm Index (DSI): A method for monitoring broadscale wind erosion using meteorological records. *Aeolian Research* 12: 29-40. DOI: 10.1016/j.aeolia.2013.10.004

62. Baddock M., Parsons K., Strong C., Leys J., McTainsh G., 2015. Drivers of Australian dust: a case study of frontal winds and dust dynamics in the lower Lake Eyre Basin. *Earth Surface Processes and Landforms* 40: 1982-1988. DOI: 10.1002/esp.3773

63. Anisimov, A., Axisa, D., Kucera, P., et al., 2018, Observations and Cloud-Resolving Modeling of Haboob Dust Storms Over the Arabian Peninsula, *Journal of Geophysical Research: Atmospheres*, https://doi.org/10.1029/2018JD028486

Appendix

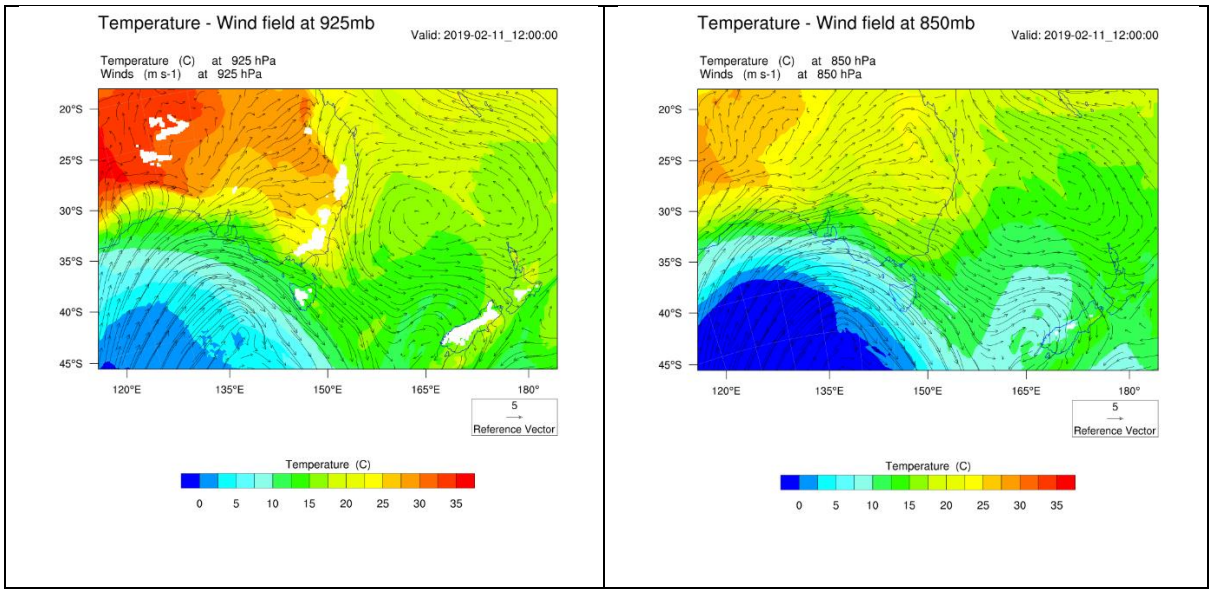

Preprints (www.preprints.org) | NOT PEER-REVIEWED | Posted: 27 October 2019 doi:10.20944/preprints201910.0304.v1

Peer-reviewed version available at *Atmosphere* **2019**, *10*, 653; doi:10.3390/atmos10110653

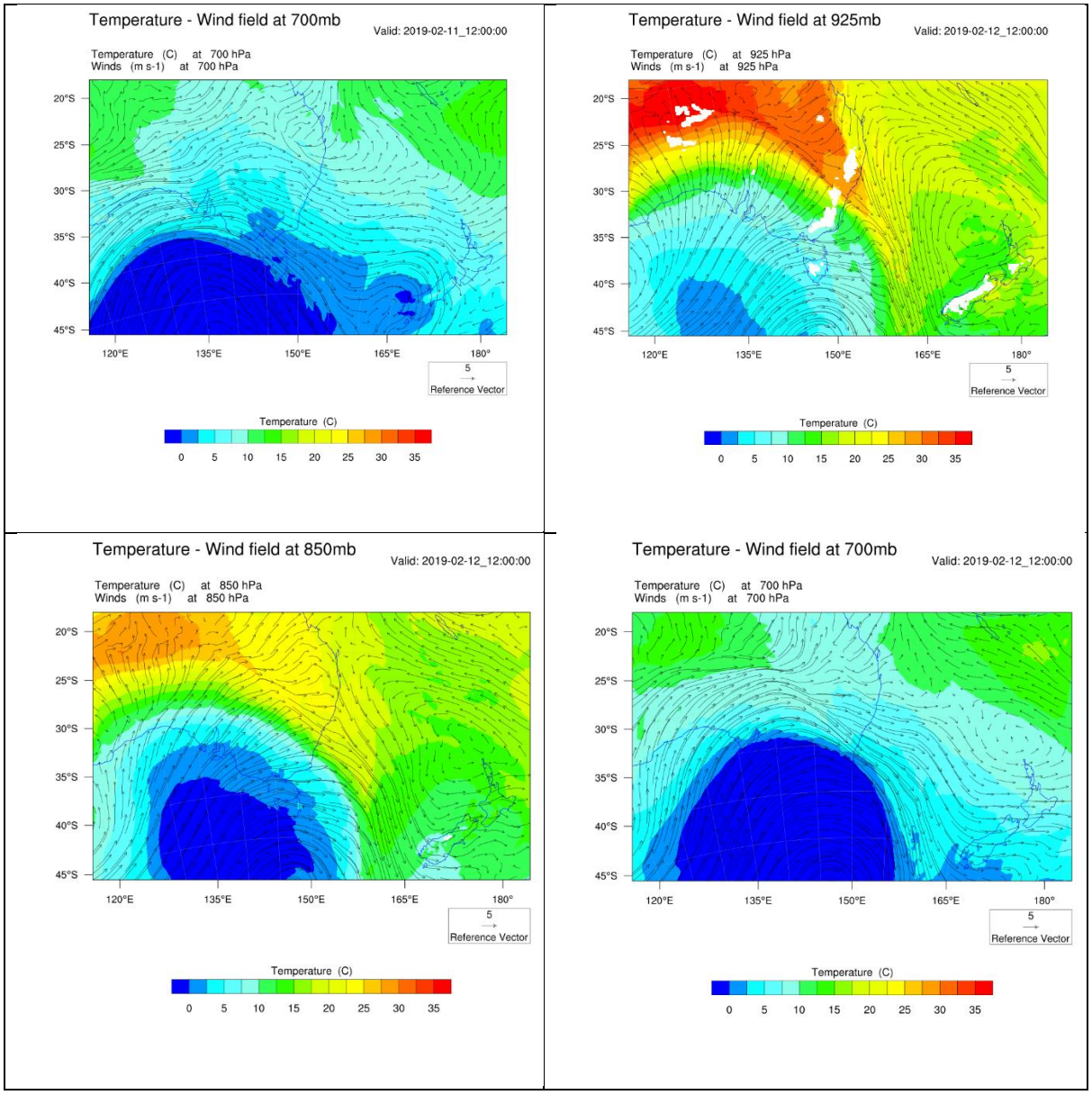

Figure A1 - Temperature and wind field at 950mb, 850mb and 700mb on 11/2/2019 12:00 UTC and 12/2/2019 12:00 UTC

Preprints (www.preprints.org) | NOT PEER-REVIEWED | Posted: 27 October 2019 doi:10.20944/preprints201910.0304.v1

Peer-reviewed version available at *Atmosphere* **2019**, *10*, 653; doi:10.3390/atmos10110653

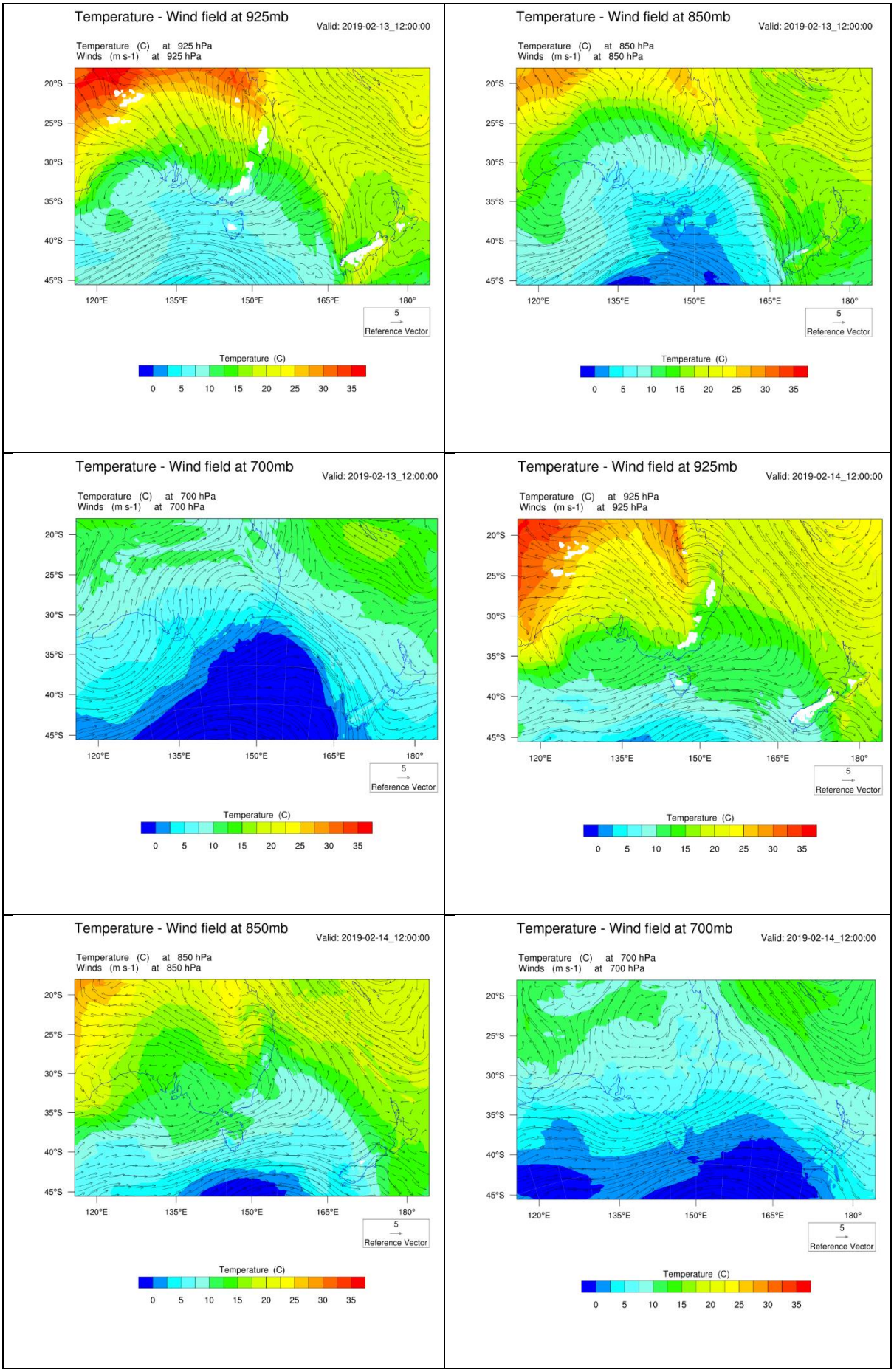

Preprints (www.preprints.org) | NOT PEER-REVIEWED | Posted: 27 October 2019 doi:10.20944/preprints201910.0304.v1

Peer-reviewed version available at Atmosphere 2019, 10, 653; doi:10.3390/atmos10110653

Figure A2 – Temperature and wind field at 950mb, 850mb and 700mb on 13/2/2019 12:00 UTC and 14/2/2019 12:00 UTC

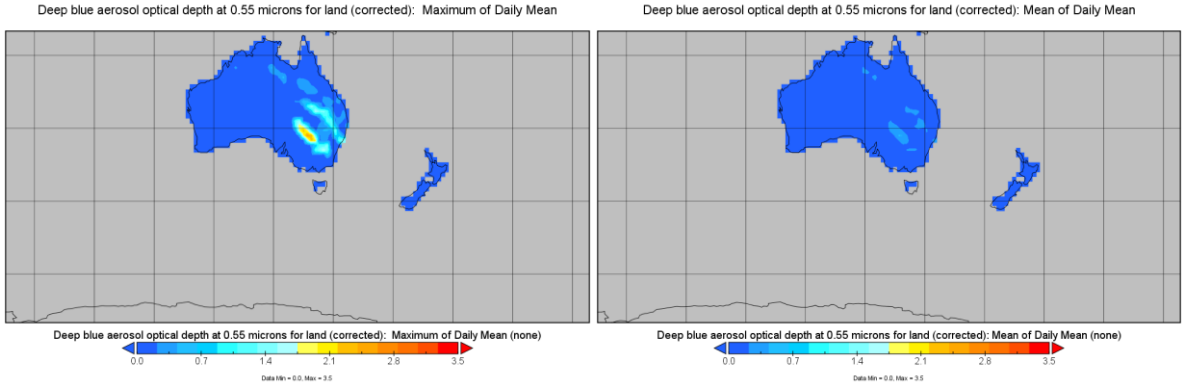

(a)

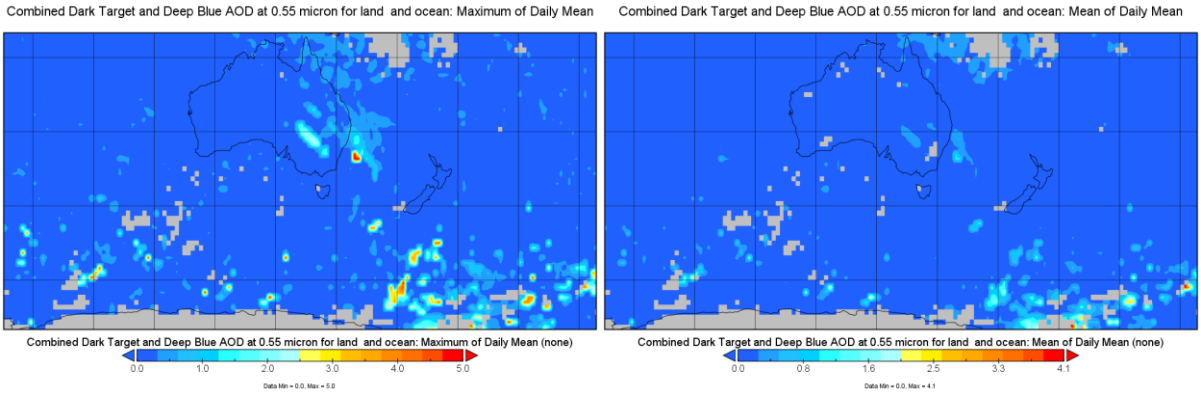

(b)

Figure A3 – (a) Aqua MYD08-E3 maximum and mean of daily mean on land for the period from 10 to 13 February 2019 and (b) Aqua MYD08-E3 Combined Dark Target (ocean) and Deep Blue (land) maximum and mean of daily mean for the period from 10 to 17 February 2019.

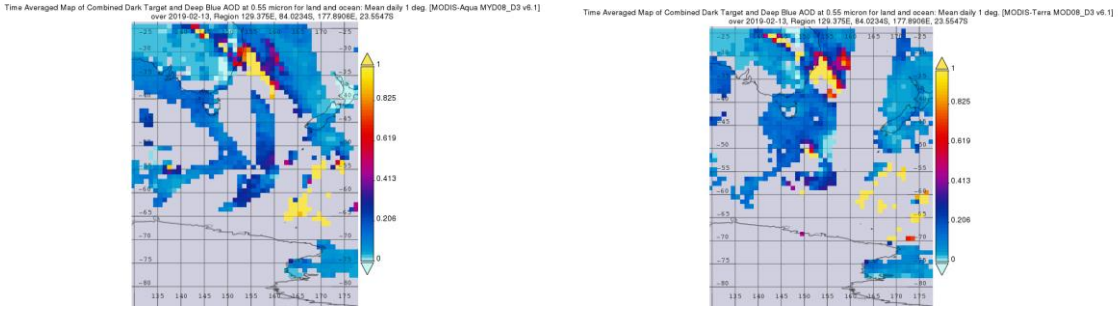

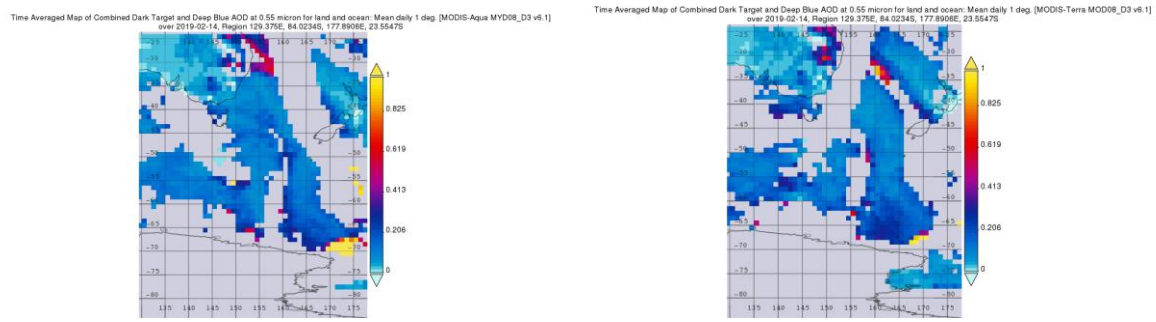

Figure A4 – Daily average AOD for 13 (top) and 14 February 2019 (bottom) as measured by MODIS Aqua (left) and Terra (right) between Australia, New Zealand and Antarctica (https://giovanni.gsfc.nasa.gov/)